ARTICLE

MicroRNA-99a mimics inhibit M1 macrophage phenotype and adipose tissue inflammation by targeting TNFα

Anant Jaiswal[1], Sukka Santosh Reddy[2], Mohita Maurya[1], Preeti Maurya[2] and Manoj Kumar Barthwal[1]

In human adipose tissue and obesity, miR-99a expression is negatively correlated with inflammation. Therefore, the present study investigated the role of miR-99a in macrophage phenotype activation and adipose tissue inflammation. M2 BMDMs showed a significant increase in miR-99a expression when compared to the M0 and M1 phenotypes. Phenotype-switching experiments established an association between upregulated miR-99a expression and the M2 phenotype. Overexpression of miR-99a prevented M1 phenotype activation and attenuated bactericidal activity. Likewise, knockdown of miR-99a abolished M2 phenotype activation. By means of in silico target prediction tools and a luciferase reporter assay, TNFα was identified as a direct target of miR-99a. Knockdown of TNFα recapitulated the effect of miR-99a overexpression in M1 BMDMs. In a db/db mice model, miR-99a expression was reduced in eWAT and F4/80$^+$ ATMs. Systemic overexpression of miR-99a in db/db mice attenuated adipocyte hypertrophy with increased CD301 and reduced CD86 immunostaining. Flow cytometry analysis also showed an increased M2 and a reduced M1 macrophage population. Mimics of miR-99a also improved the diabetic dyslipidemia and insulin signaling in eWAT and liver, with an attenuated expression of gluconeogenesis and cholesterol metabolism genes in the liver. Furthermore, adoptive transfer of miR-99a-overexpressing macrophages in the db/db mice recapitulated in vivo miR-99a mimic effects with increased M2 and reduced M1 macrophage populations and improved systemic glucose, insulin sensitivity, and insulin signaling in the eWAT and liver. The present study demonstrates that miR-99a mimics can regulate macrophage M1 phenotype activation by targeting TNFα. miR-99a therapeutics in diabetic mice reduces the adipose tissue inflammation and improves insulin sensitivity.

Cellular & Molecular Immunology (2019) 16:495–507; https://doi.org/10.1038/s41423-018-0038-7

INTRODUCTION

The macrophage phenotype can regulate adipose tissue inflammation and insulin resistance. Macrophage-specific deletion of proinflammatory mediators inhibits M1 polarization and reduces adipose tissue inflammation.[1,2] Similarly, M2 phenotype regulators, such as IRF4 and PPARγ, promote an anti-inflammatory response and decrease adipose tissue inflammation.[3,4] The genetic deletion of cells such as CD8$^+$ T cells also reduces macrophage recruitment and inflammation in adipose tissue.[5] Conversely, the activation of NKT cells enhances adipose tissue M2 polarization and improves insulin sensitivity.[6]

Whole-genome studies have theorized that there is an essential role for noncoding RNAs in the regulation of insulin resistance and T2DM.[7] Among the noncoding RNAs, microRNAs (miRNAs) are a group of small endogenous noncoding RNAs that regulate gene expression at the posttranscriptional level by binding to the 3′-untranslated region of target mRNAs.[8] Moreover, several miRNAs have been identified that play an essential role in macrophage function and adipose tissue inflammation.[9,10] In therapeutic interventions, a number of miRNAs have also progressed from preclinical to phase-I and phase-II trials.[11]

Recent studies have demonstrated the role of miR-99a as a tumor suppressor in some types of cancer, as well as a negative regulator of cardiac hypertrophy.[12,13] Additionally, miR-99a expression negatively correlates with fatty acids, inflammatory mediators, and obesity in human adipose tissue.[14,15] This suggests that miR-99a might be a potential regulator of adipose tissue inflammation.

Emerging evidence also suggests that miRNAs associated in a cluster often exert similar functions in several cell types and diseases.[16] miR-99a is a known clustered miRNA and localizes in a cluster with let-7c (on Chr-21 in human and Chr-16 in murine). Let-7c is known to regulate macrophage polarization by inhibiting M1 and promoting M2 phenotype activation.[17] However, the role of miR-99a in macrophage phenotype activation is not yet known. Therefore, the current study evaluates the role of miR-99a in macrophage phenotype activation and adipose tissue inflammation.

MATERIALS AND METHODS

Cell culture and treatments

Bone marrow-derived macrophages (BMDMs) were isolated from the femur and tibia of C57BL/6J mice. Briefly, the bones were flushed with ice-cold PBS containing 20 U/ml heparin, followed by incubation with sterile 0.843% ammonium chloride solution for 10 min to lyse the erythrocytes. A single-cell suspension was obtained by straining through a 70-µm cell strainer. The cells were then plated in RPMI medium (Sigma Aldrich) supplemented with 10% FBS (Gibco) and 10 ng/ml MCSF (Peprotech) for 7 days. On the seventh day, cells were starved from MCSF for 12 h and

[1]Division of Pharmacology, Council of Scientific and Industrial Research-Central Drug Research Institute (CSIR-CDRI), Lucknow 226031 U.P., India and [2]Academy of Scientific and Innovative Research, New Delhi 110025, India
Correspondence: Manoj Kumar Barthwal (manojbarthwal@cdri.res.in)

Received: 28 November 2017 Revised: 21 April 2018 Accepted: 21 April 2018
Published online: 30 May 2018

stimulated for 24 h with 1 μg/ml LPS (Sigma-Aldrich) and either 20 ng/ml IFN-γ (Peprotech) to obtain the M1 phenotype or 20 ng/ml IL-4 (Peprotech) to obtain the M2 phenotype. In the reswitching experiments, the M1 macrophages were treated with either LPS/IFN-γ (M1 control) or IL-4 (reswitch) for 24 h. Similarly, M2 macrophages were treated with either IL-4 (M2 control) or LPS/IFN-γ (reswitch) for 24 h.[18]

Lentivirus production and transduction in BMDMs

Lentiviral particles were produced by cotransfection of lentiviral helping plasmids and a plasmid encoding the gene of interest, miR-99a (MmiR3457-MR03, GeneCopoeia), miR-scramble control (CmiR0001-MR03, GeneCopoeia), TNFα-shRNA (TRCN0000362936, Sigma-Aldrich) or scramble shRNA (SHC001) or lentiviral-miR-99a inhibitor (1020171SMN, Sigma-Aldrich) in HEK293T cells using Lipofectamine 2000 (Invitrogen). The lentiviral particles were titrated and concentrated as previously described.[19] On the sixth day, BMDMs were treated with 1.5×10^6 PFU lentiviral particles in the presence of polybrene (8 mg/ml). After 48 h, the cells were starved from MCSF and treated for 24 h with 1 μg/ml LPS and either 20 ng/ml IFN-γ for the M1 phenotype or 20 ng/ml IL-4 for the M2 phenotype.[20]

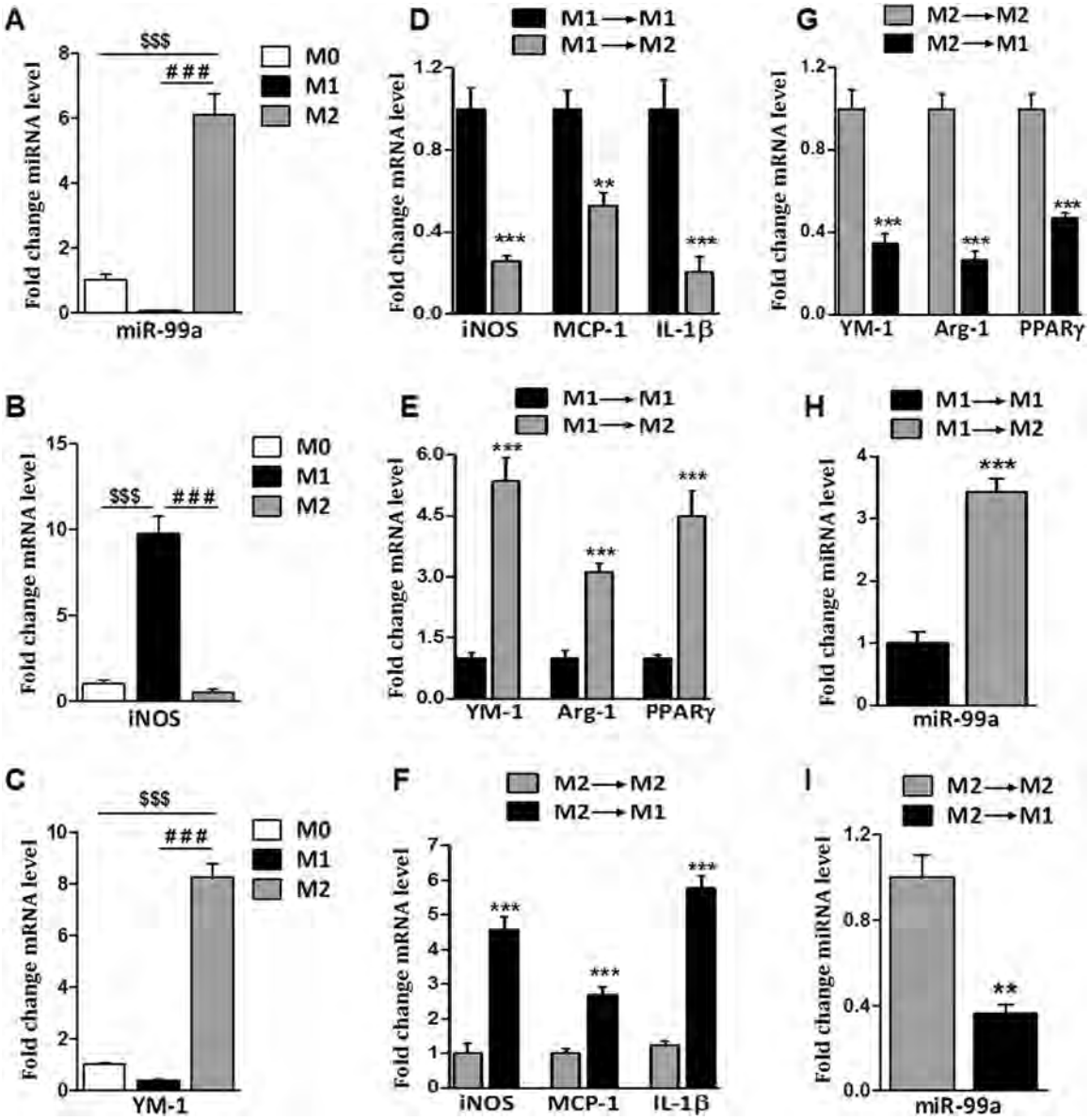

Fig. 1 miR-99a expression and macrophage phenotype activation. **a** miR-99a expression levels were measured in control (M0) or LPS/IFN-γ (M1) and IL-4 (M2)-stimulated BMDMs by Taqman-qPCR ($n = 6$). **b** iNOS mRNA expression in control (M0), LPS/IFN-γ- (M1), and IL-4 (M2)-stimulated BMDMs by qPCR ($n = 4$). **c** YM-1 mRNA expression in control (M0), LPS/IFN-γ (M1)-, and IL-4 (M2)-stimulated BMDMs by qPCR ($n = 4$). **d** iNOS, MCP-1, and IL-1β mRNA expression in M1 to M1 (control) and M1 to M2 (reswitch) BMDMs by qPCR ($n = 6$). **e** YM-1, ARG-1, and PPARγ mRNA expression in M1 to M1 (control) and M1 to M2 (reswitch) BMDMs by qPCR ($n = 6$). **f** iNOS, MCP-1, and IL-1β mRNA expression in M2 to M2 (control) and M2 to M1 (reswitch) BMDMs by qPCR ($n = 6$). **g** YM-1, ARG-1, and PPARγ mRNA expression in M2 to M2 (control) and M2 to M1 (reswitch) BMDMs by qPCR ($n = 6$). **h** miR-99a expression levels in M1 to M1 (control) and M1 to M2 (reswitch) BMDMs by Taqman-qPCR ($n = 6$). **i** miR-99a expression levels in M2 to M2 (control) and M2 to M1 (reswitch) BMDMs by Taqman-qPCR ($n = 6$). Data are presented as the mean ± SEM of 4–6 independent experiments. $^{**}P < 0.01$, $^{***}P < 0.001$, $^{\#\#\#}P < 0.001$ vs. M1 and $^{\$\$\$}P < 0.001$ vs. M0

Adoptive transfer miR-99 transduced BMDMs in *db/db* mice

BMDMs were isolated from *db/db* animals and cultured for 7 days in RPMI medium in the presence of MCSF. For miR-99a overexpression, BMDMs were transduced with either miR-99a or miR-scramble lentiviral particles, as described above. The transduction efficiency was regularly assessed by qRT-PCR and microscopy. For the in vivo adoptive transfer experiments, transduced BMDMs were smoothly transferred to a culture tube and maintained in PBS until injection into the animal. A total of 1×10^6 cells per mice were administered for six consecutive days through tail-vein injection.[21] Random and fasting glucose levels were measured after 3 days and 10 days from the first injection, respectively. An intraperitoneal glucose tolerance test (ipGTT) and an insulin tolerance test (ITT) were performed before the first injection and at 4 days after the last injection in the group.

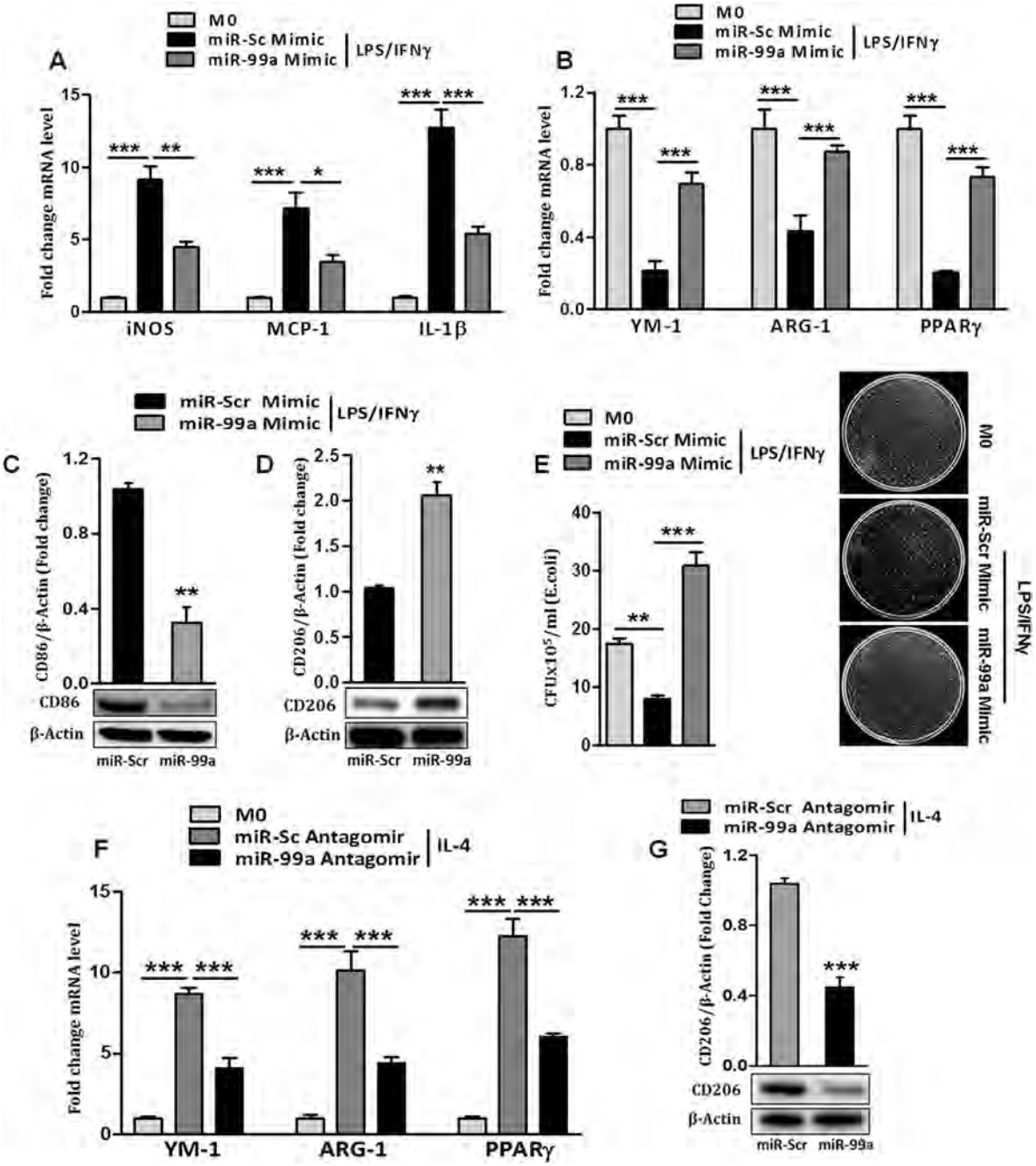

Fig. 2 Effect of miR-99a modulation on M1 and M2 macrophage phenotype and function. BMDMs were infected with 1.5×10^6 PFU lentivirus containing miR-99a/miR- scramble or miR-99a antagomir/miR-scramble antagomir, and after 72 h, the cells were stimulated with vehicle (M0, control) or LPS/IFN-γ (M1) or IL-4 (M2) for 24 h. **a** iNOS, MCP-1, and IL-1β mRNA expression. **b** YM-1, ARG-1, and PPARγ mRNA expression ($n = 6$). **c** CD86 protein expression. **d** CD206 protein expression ($n = 3$). **e** Bacterial colonies were counted and CFUs of *E. coli* were determined in miR-99a- or miR-scramble-treated M1 and control M0 ($n = 6$) cells. **f** YM-1, ARG-1, and PPARγ mRNA expression in miR-99a antagomir- or miR-scramble antagomir-treated M2 and control M0 cells by qPCR ($n = 6$). **g** CD206 protein expression in miR-99a antagomir- or miR-scramble antagomir-treated M2 and control M0 cells by western blot ($n = 3$). Data are presented as the mean ± SEM of 3–6 independent experiments. $^*P < 0.05$; $^{**}P < 0.01$; $^{***}P < 0.001$ vs. miR-scramble. Blots represent at least one of three similar experiments

ATM quantification and sorting by flow cytometry

After the desired treatment, the epididymal white adipose tissue (eWAT) from 10- to 12-week-old male *db/db* mice and control *db/+* mice was excised, rinsed in 1×DPBS (PBS with $CaCl_2$ and 0.5% BSA), and minced and digested with collagenase solution (collagenase type-II, Sigma-Aldrich, 1 mg/ml in DPBS) at 37 °C for 20 min with shaking. The digested solution was strained through a 100-µm filter to obtain a single-cell suspension. Floating adipocytes and the SVF pellet were separated by centrifugation at 500 × *g* for 5 min. The SVF pellet was suspended in ACK buffer to lyse the erythrocytes, followed by washing with DPBS and centrifugation. For flow cytometry, the SVF pellet was resuspended in FACS buffer (DPBS, 2 mM EDTA, and 1% FBS) and stained with the following conjugated antibodies for 15 min at 4 °C: F4/80-PE (12-4801, eBioscience), CD11b-PE-cyanine7 (25-0112, eBioscience), CD11c-eFluor450 (48-0114, eBioscience), CD206-AlexaFluor®647 (565250, BD-Bioscience), and Ly6C-APC (17-5932, eBioscience). After staining, the samples were washed with FACS buffer and analyzed by FACS Diva software on a FACS Aria (Becton Dickinson, USA). For cell sorting, equal numbers of F4/80$^+$CD11b$^+$CD11c$^+$CD206$^-$ (M1) and F4/80$^+$CD11b$^+$ CD11c$^-$ CD206$^+$ (M2) cells were quantified and sorted for RNA extraction.[22]

Bactericidal activity of BMDMs

The bacteria-killing capacity of BMDMs was performed as previously described.[17] miR-99a or miR-scramble-overexpressed BMDMs were stimulated with 1 µg/ml LPS and 20 ng/ml IFN-γ for the M1 phenotype. After 24 h, the cells were incubated with 1 × 10^6 CFU/ml *Escherichia coli* (pCMV6$^-$vector) in 96-well plates. The plates were centrifuged at 400 × g for 5 min and incubated for 60 min at 37 °C. The supernatant from each well was collected and subjected to 100-fold dilutions. A total of 100 µl of the diluted supernatant was plated on Luria broth agar plates. The plates were incubated at 37 °C overnight. Bacterial colonies were counted and expressed as CFU/ml. CFU/ml = number of colonies × dilution factor/volume of the plated diluted supernatant.

microRNA isolation and TaqMan RT-PCR assay

Total RNA, including miRNA, was isolated from cells or tissues utilizing the miRVana™ miRNA isolation kit (AM1561, Ambion, Lifetech) under RNase-free conditions, according to the manufacturer's protocol. Total RNA was eluted with preheated nuclease-free water. The purity of the RNA was assessed by a NanoDrop™2000c spectrophotometer (Thermo Scientific), and high-quality RNA (A260/280 ratio > 1.8) preparations were used for further processing. miRNA expression was measured using the Taqman® Single miRNA assay (assay ID; 000435, LifeTech) as per the manufacturer's protocol. Briefly, 500 ng of total RNA was reverse transcribed using the TaqMan miRNA Reverse Transcription Kit (4366596, LifeTech) with 3 µl of miRNA-specific RT primers on a thermal cycler (Applied Biosystems). Real-time PCR was performed on QuantStudio™12K Flex Real-Time PCR System (Applied Biosystems®, LifeTech) using TaqMan® Universal PCR Master Mix (4304437, LifeTech) with miRNA-specific TM primers. miRNA expression was normalized to U6snRNA. The fold change of miRNA expression was calculated by QuantStudio™12K Flex Real-Time software v1.2.2 (Applied Biosystems®, LifeTech).[23]

mRNA isolation and qPCR

mRNA isolation and qPCR were performed as previously described.[24] Briefly, total RNA was isolated from BMDMs or tissues with TRIzol™ Reagent (Thermo Fisher Scientific) or for sorted ATMs, with an RNeasy Mini Kit (74104-QIAGEN) and reverse transcribed

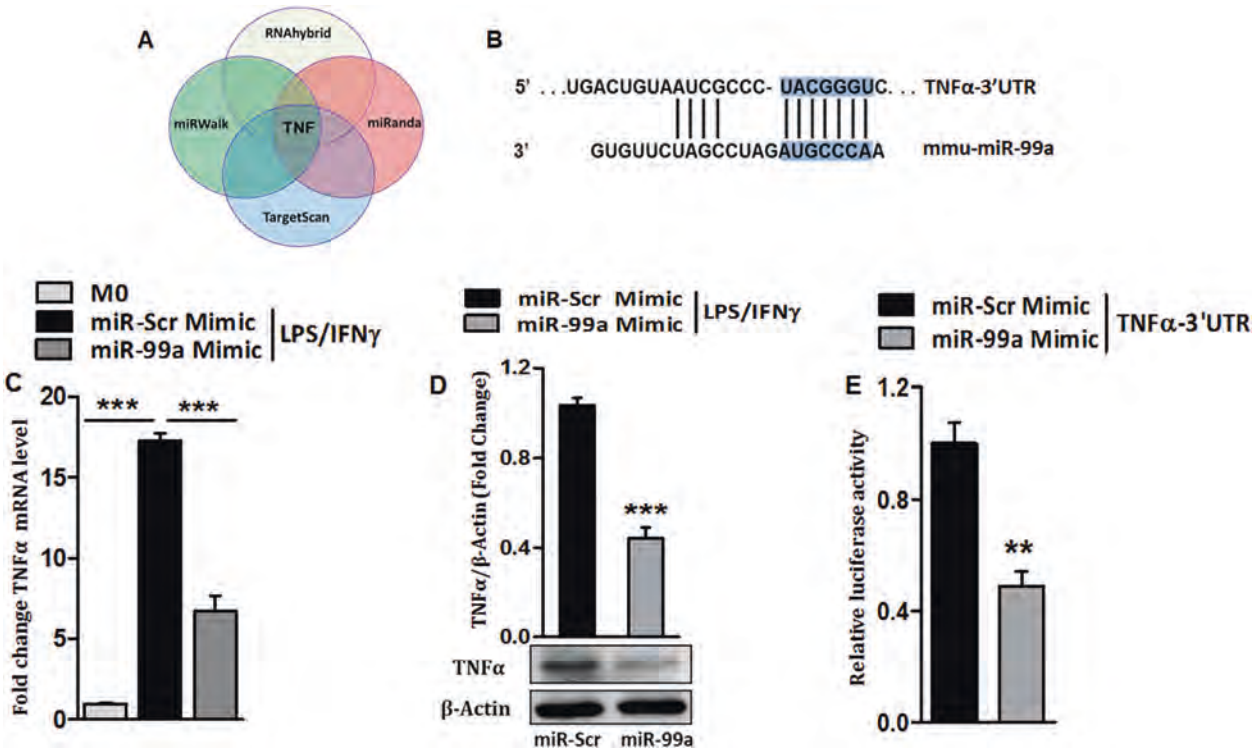

Fig. 3 miR-99a targets TNFα. **a** In silico, four different target prediction software packages predicted TNFα to be the target of miR-99a. **b** Predicted miR-99a binding site in the 3′ untranslated region (UTR) of TNFα seed sequences. **c** TNFα mRNA expression in control (M0) or miR-99a- and miR-scramble-pretreated and LPS/IFN-γ (M1)-stimulated BMDMs by qPCR ($n = 6$). **d** TNFα protein expression in miR-99a- and miR-scramble-pretreated and LPS/IFN-γ (M1)-stimulated BMDMs, as assessed by western blotting ($n = 3$). **e** Reporter constructs with a 3′-UTR region containing the binding site of TNFα were cotransfected with miR-scramble or miR-99a in HEK293T cells. Luciferase activity was analyzed after 72 h ($n = 6$). Data are presented as the mean ± SEM of six independent experiments. $^{**}P < 0.01$; $^{***}P < 0.001$ vs. miR-scramble

with a high-capacity cDNA reverse transcription kit (4368814, LifeTech). Real-time qPCR was performed in a LightCycler® 480II system (Roche Applied Science, USA) using gene-specific primers and SYBR Green reagent. Gene expression was normalized to 18SrRNA. The primer sequences are listed in Supplementary Table I.

In silico target prediction analysis

The prediction analysis of miRNA binding to the TNF 3′-UTR was performed by using the miRwalk databases utilizing different algorithms, including, miRwalk, miRanda, DIANA-mT, RNA22, TargetScanv6.2, and miRDB.[25] Of the six algorithms, four considered TNF to be a potential target for miR-99a. To determine the individual score of identity, conserved miRNAs with good mirSVR scores were selected using the miRanda algorithm.

Luciferase reporter assay

The 3′-UTR of TNFα (MmiT077890-MT06, GeneCopoeia) and miR-99a (MmiR3457-MR03, GeneCopoeia) or miR-scramble control (CmiR0001-MR03, GeneCopoeia) were cotransfected by Lipofectamine 2000 (Invitrogen) into HEK293T cells. The firefly and renilla luciferase activity in the cell lysates was measured at 72 h post transfection using a dual-luciferase assay system (E1910; Promega) according to the manufacturer's protocol. The data were normalized as the ratio of renilla/firefly luciferase activity.[26]

Western blot assay

After the desired treatment in *db/db* animals, liver and adipose tissues were collected and lysed in RIPA lysis buffer. The membranes were probed overnight at 4 °C with primary antibodies including p-IRS-1^{Ser307} (sc-33956), IRS-1 (C-20, sc-559), p-Akt^{Ser473} (D9E, 4060; CST), Akt (11E7, 4685; CST), and GAPDH (ABS16; MERK), followed by incubation with specific secondary HRP-conjugated antibody at RT for 2 h. Phosphorylation was normalized to the respective total protein expression. The bands were detected by ECL, and the intensity was quantified by Image Quant, LAS 4000 (Amersham, MA).[27]

Animal experiments

All animal experiments were approved by the Institutional Animal Ethical Committee, Council for Scientific and Industrial Research-Central Drug Research Institute (CSIR-CDRI), as per guidelines of the Committee for the Purpose of Control and Supervision of Experiments on Animals (CPCSEA). The 10–12-week-old male diabetic (C57BLKs-*db/db*) and nondiabetic control (C57BLKs-*db/+*) mice were maintained on a 12-h light–dark cycle with ad libitum access to food and water at the Council of Scientific and Industrial Research-Central Drug Research Institute (CSIR-CDRI). A total of 1×10^7–10^8 lentiviral particles containing miR-99a or miR-scramble control were injected intravenously (once per day) for three consecutive days in 6–8 male *db/db* mice per group using Lipofectamine 2000 (Life Technologies). Random and fasting glucose levels were measured after 3 days and 10 days from the first injection, respectively. An intraperitoneal glucose tolerance test (ipGTT) and an insulin tolerance test (ITT) were performed before the first injection and at 7 days after the last lentiviral injection in the group.[28]

ipGTT and ITT

ipGTT and ITT were performed after 12 h or 6 h of fasting, respectively. The mice were intraperitoneally administered glucose (2 g/kg for ipGTT) or human insulin (0.75 IU/kg for ITT, Eli Lilly, Indianapolis, IN) for the respective tests. Blood glucose was monitored at the indicated time points with an Accu-Chek Active blood glucometer. The area under the curve (AUC) for ipGTT and ITT was calculated.[29]

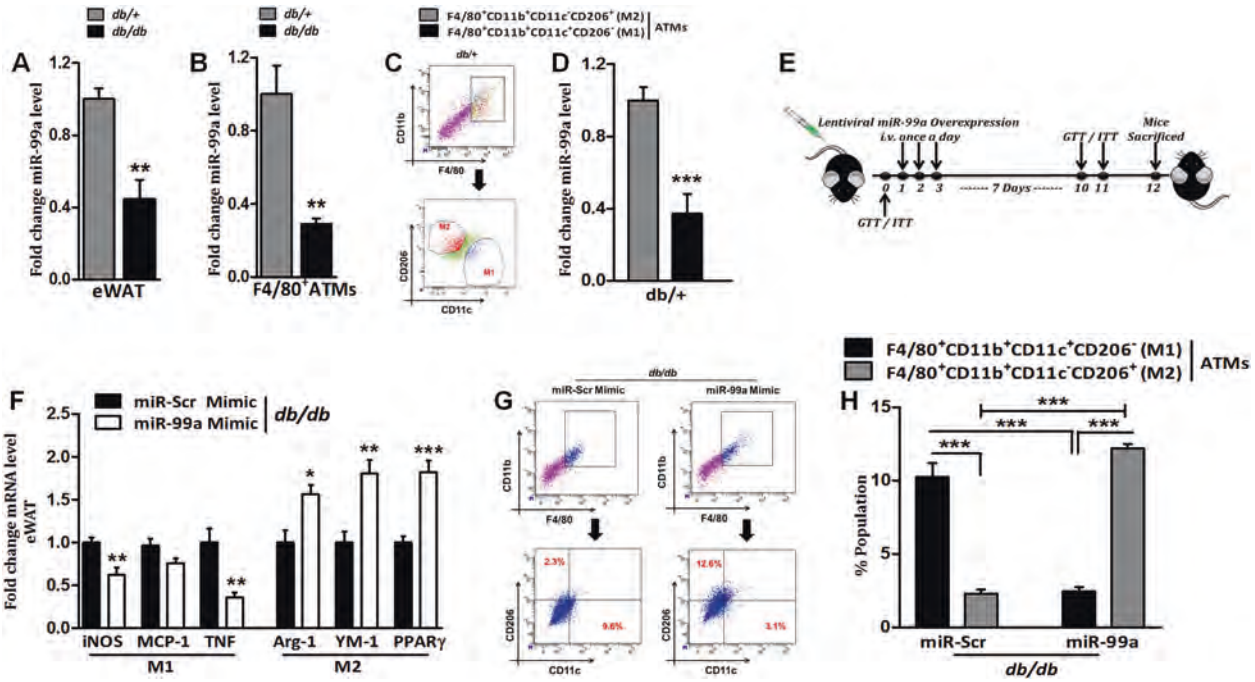

Fig. 4 miR-99a overexpression modulates ATM phenotype. miR-99a expression was measured in **a** eWAT **b** F4/80$^+$-sorted ATMs by Taqman-qPCR ($n = 6$). **c** The dot plot represents labeling of F4/80$^+$ CD11b$^+$CD11c$^+$ CD206$^-$(M1) and F4/80$^+$CD11b$^+$CD11c$^-$CD206$^+$(M2) ATMs sorted from *db/+* mice. **d** miR-99a expression in M1- and M2-sorted ATMs from *db/+* mice by Taqman-qPCR ($n = 6$). **e** Treatment regime of miR-99a or miR-scramble lentivirus and timeline for the measurement of parameters. **f** *db/db* mice were treated with miR-99a or miR-scramble, and mRNA expression of M1 (iNOS, MCP-1, and TNFα) and M2 (YM-1, ARG-1, and PPARγ) macrophage signature genes was determined in total eWAT by qPCR ($n = 6$). **g** Dot plot represents labeling of F4/80$^+$CD11b$^+$CD11c$^+$CD206$^-$(M1) and F4/80$^+$CD11b$^+$CD11c$^-$CD206$^+$(M2) ATMs from miR-99a- or miR-scramble-treated *db/db* mice by flow cytometry ($n = 6$). **h** Bar diagram represents quantification of figure **g**. Data are presented as the mean ± SEM of at least six mice per group from three independent experiments, $^*P < 0.05$; $^{**}P < 0.01$; $^{***}P < 0.001$

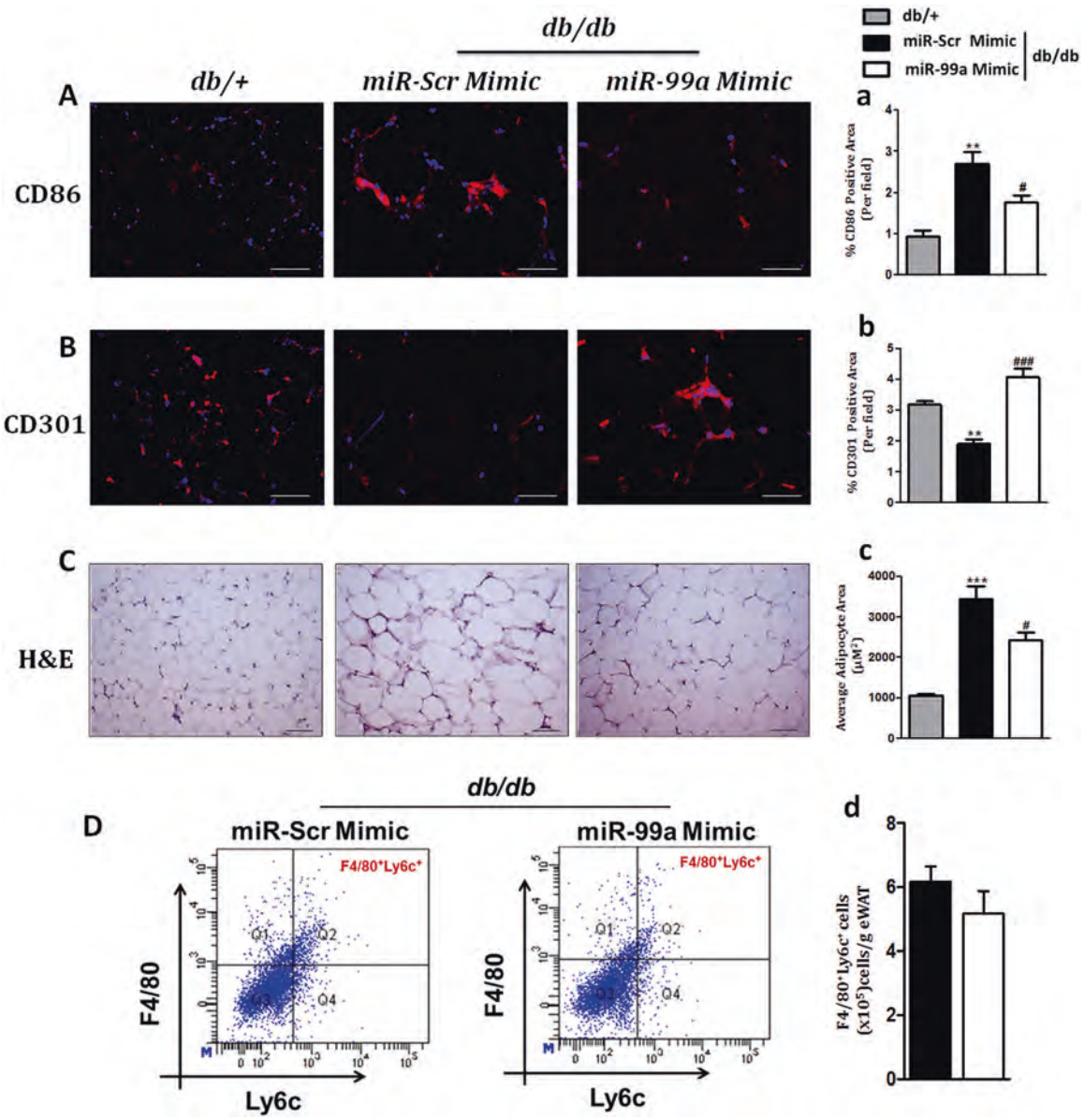

Fig. 5 Overexpression of miR-99a regulates macrophage phenotype activation. Representative microscopic images of adipose tissue sections derived from *db/+* and miR-99a- or miR-scramble-treated *db/db* mice. **A** CD86 staining depicting M1 macrophage and **B** CD301 staining depicting M2 macrophages, magnification; ×40, **C** hematoxylin and eosin (H&E) staining depicting adipocyte area, magnification; ×20, scale bars = 50 μm. The results are representative of adipose tissue sections from at least six animals from each group. **D** Dot plot represents labeling of $F4/80^{+}Ly6c^{+}$ ATMs by flow cytometry from miR-99a- or miR-scramble mimic-treated *db/db* mice ($n = 6$). Bar diagram showing the number of $F4/80^{+}Ly6c^{+}$ ATMs/gram eWAT shown in **D**. Bar diagrams **a**, **b**, and **c** are quantifications of images **A**, **B**, and **C**, respectively, as described in the methods. Data are presented as the mean ± SEM of at least six mice per group from three independent experiments. $^{**}P < 0.01$; $^{***}P < 0.001$ *db/+* vs. miR-scramble *db/db*, and $^{\#}P < 0.05$; $^{\#\#\#}P < 0.001$ miR-scramble- vs. miR-99a-treated *db/db*

Plasma measurements

Mice fasted for 6 h, and plasma was collected prior killing. Circulatory lipids, total cholesterol (TC), triglycerides (TG), and low- and high-density lipoprotein (LDL, HDL) were estimated using commercial kits (Randox, UK). The insulin levels were measured using ELISA kits (Millipore, USA). The HOMA-IR functionality was calculated as per the previously used formulae.[30]

Hematoxylin and eosin (H&E) stain and immunohistochemistry

Formalin-fixed tissues were processed in graded concentrations of ethanol followed by xylene prior to liquid paraffin infiltration. The paraffin-embedded tissue blocks were sectioned (4–5-μm slices), and HE-stained images were captured in the bright-field mode using an upright microscope (DM5000, Leica Microsystems, Germany). Fifty fields were scanned for each sample, and ten random fields were analyzed. The number of adipocytes was counted, and their area was obtained. The morphometric results were quantified using the ImageJ software (Image Processing and Analysis in Java, public domains).[31] The immunofluorescence analyses of CD86 (1:200, sc-28347; Santa Cruz) and CD301 (1:400, MCA2392; Bio-Rad) were conducted after deparaffinization, as previously described.[32] Secondary antibodies were then applied (AlexaFluor 594, A1105; Invitrogen), followed by DAPI (D9542, Sigma). The sections were mounted and visualized using a fluorescence microscope (DM6000, Leica Microsystems, Germany). Macrophages were counted in a randomly selected area, and cell types showing cytoplasmic staining were considered positive for quantitative analysis. The number of macrophages per area was

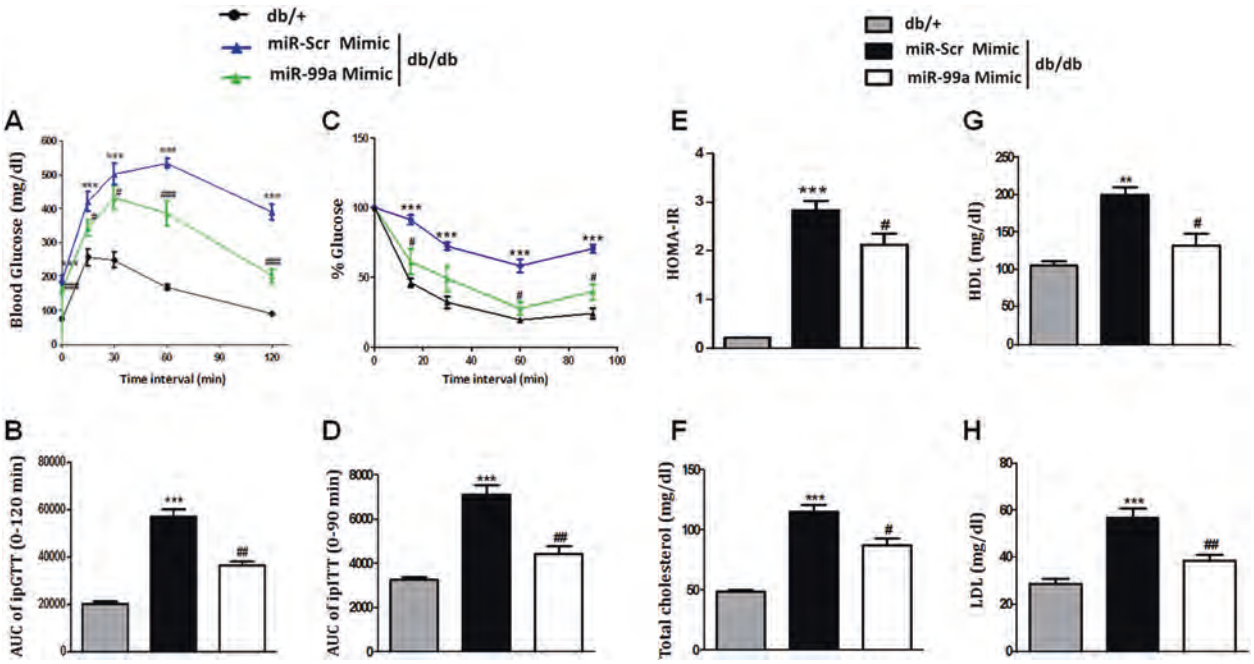

Fig. 6 Overexpression of miR-99a regulates systemic glucose, insulin tolerance, and dyslipidemia. Post 7 days from the last miR-99a or miR-scramble injection, **a** intraperitoneal glucose tolerance test (ipGTT) and **b** the area under the curve (AUC) during ipGTT, **c** insulin tolerance test (ITT), **d** the area under the curve (AUC) during ITT, **e** HOMA-IR, **f** total cholesterol, **g** high-density lipoprotein (HDL), and **h** low-density lipoprotein (LDL). Data are presented as the mean ± SEM of 9–12 mice per group from three independent experiments. $^{**}P < 0.01$, $^{***}P < 0.001$ *db/+* vs. miR-scramble-treated *db/db*, and $^{\#}P < 0.05$; $^{\#\#}P < 0.01$; $^{\#\#\#}P < 0.001$; miR-scramble- vs. miR-99a-treated *db/db*

calculated using the following formula: number of positive cells per field/adipocyte area per field.[33] The images were quantified using ImageJ.

Statistical analysis

The experimental values in the results are expressed as the mean ± SEM. All experiments were performed at least three times. The significance of the difference between groups was analyzed by performing one-way analysis of variance (ANOVA), followed by the Bonferroni post hoc test. The significance level for the Bonferroni multiple-comparison test was set to 0.05 for three or more groups. The difference between two groups was compared using the unpaired Student's *t*-test, and a *p*-value < 0.05 was considered to be statistically significant.

RESULTS

miR-99a regulates M1 macrophage phenotype activation

To understand the correlation between miR-99a expression and macrophage phenotype, we first estimated the levels of miR-99a using a Taqman RT-PCR assay in unstimulated (M0), LPS/IFN-γ-stimulated classically activated (M1), and IL-4-treated alternatively activated (M2) bone marrow-derived macrophages (BMDMs). Expression of miR-99a was significantly higher in the M2 macrophages (~6-fold) compared to M0 and M1 (Fig. 1a). LPS/IFN-γ stimulation induced a significant increase in the mRNA expression of iNOS (~10-fold) when compared to M2 and M0 macrophages, indicating activation of the M1 phenotype (Fig. 1b). Concurrently, IL-4-induced macrophages showed a significant increase in YM-1 mRNA expression (~8-fold) when compared to M1 and M0 macrophages (Fig. 1c), indicating M2 phenotype activation. To assess whether miR-99a expression is regulated during macrophage phenotype activation, macrophage phenotype reswitch experiments were performed. M1 or M2 BMDMs were reconverted into the M2 or M1 type by treatment with IL-4 or LPS/IFN-γ, respectively. Successful reswitching of M1 macrophages into M2 by IL-4 was confirmed since a significant decrease in iNOS, MCP-1, and IL-1β mRNA expression (Fig. 1d), and a significant increase in YM-1, ARG-1, and PPARγ mRNA expression (Fig. 1e) was observed when compared to control M1 macrophages. Similarly, the reswitching of M2 macrophages into M1 after LPS/IFN-γ stimulation induced a significant increase in iNOS, MCP-1, and IL-1β mRNA expression (Fig. 1f) and a significant decrease in YM-1, ARG-1, and PPARγ mRNA expression (Fig. 1g) when compared to control M2 macrophages. Furthermore, reswitching of the M1 macrophage phenotype into M2 significantly increased miR-99a expression (3.5-fold, Fig. 1h), and reswitching of the M2 macrophage phenotype to M1 significantly reduced miR-99a expression (2.5-fold, Fig. 1i), suggesting the modulation of miR-99a expression with macrophage phenotype. The enhanced expression of miR-99a in M2- and M1-derived M2 macrophages suggested the role of this miRNA in M2 phenotype activation. To validate this, we infected BMDMs with lentivirus containing miR-99a or miR-scramble, followed by stimulation with LPS/IFN-γ for M1 phenotype activation. The overexpression of miR-99a was confirmed by qPCR (Fig. S1A). Overexpression of miR-99a significantly reduced the M1 markers iNOS, MCP-1, and IL-1β (Fig. 2a) and enhanced the expression of the M2 markers, YM-1, ARG-1, and PPARγ (Fig. 2b), in LPS/IFN-γ-stimulated BMDMs when compared to miR-scramble-treated BMDMs. Similar results were obtained at the protein level where a significant decrease in CD86 expression (Fig. 2c) and an enhanced CD206 expression were observed after infecting with miR-99a mimics when compared to miR-scramble (Fig. 2d). These data suggest that miR-99a plays a critical role in inhibiting M1 phenotype activation. Next, to test whether changes in the phenotype also affected the macrophage function, the bactericidal activity of LPS/IFN-γ-stimulated BMDMs was assessed after treatment with miR-99a or miR-scramble mimics.

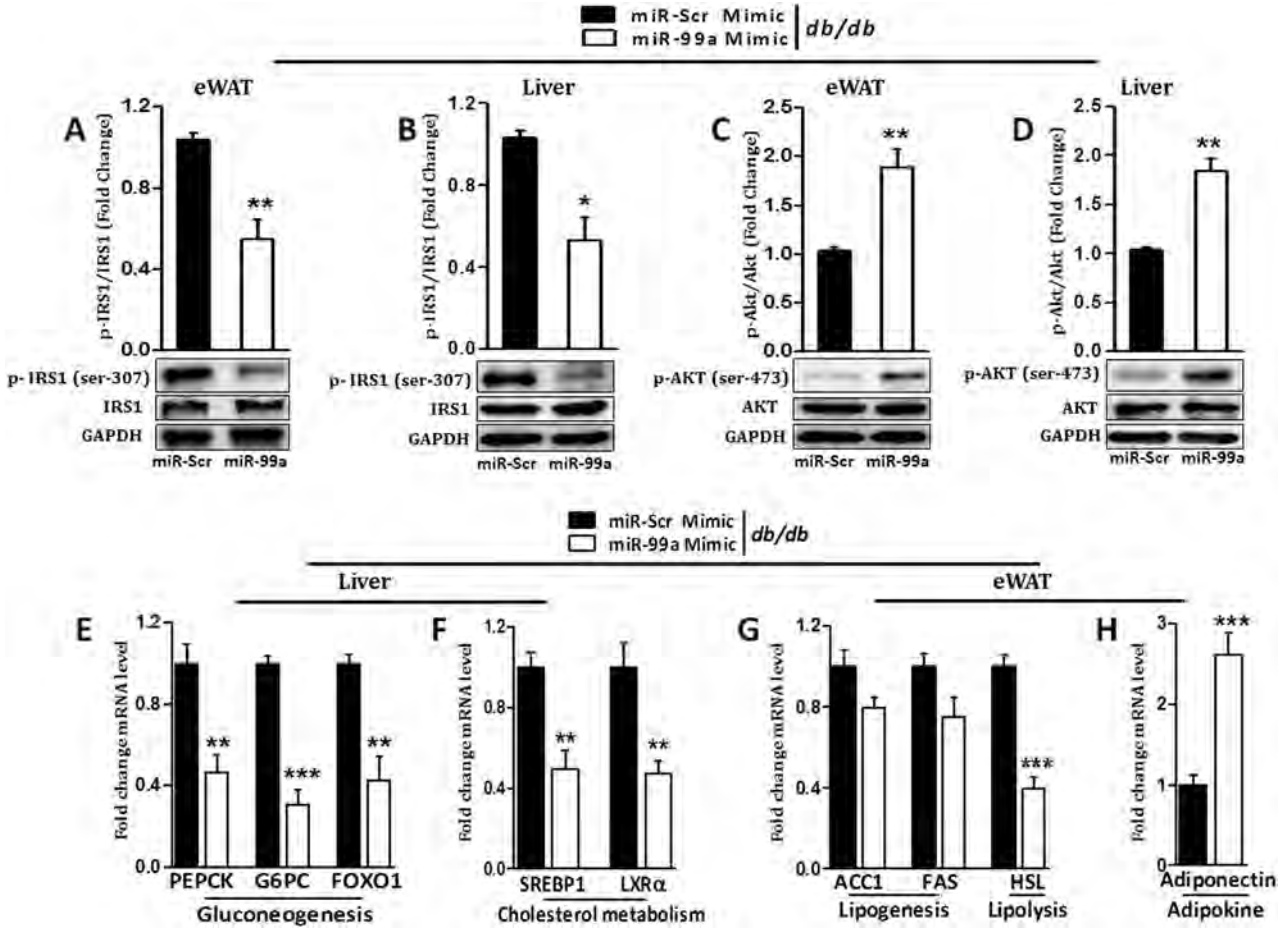

Fig. 7 Overexpression of miR-99a improves insulin signaling and glucose and lipid metabolism in *db/db* mice. Adipose tissue and liver samples were collected from *db/db* mice treated with miR-99a or miR-scramble and western blotting was performed to detect the levels of **a** p-IRS-1 (Ser-307) and IRS-1 in eWAT. **b** p-IRS-1 (Ser-307) and IRS-1 in liver. **c** p-AKT (Ser-473) and AKT in eWAT. **d** p-AKT (Ser-473) and AKT in liver. Phosphorylation of IRS-1 and AKT was normalized to their respective total proteins. The bar diagram shows the quantification of the blots from at least three independent experiments. GAPDH was used as a loading control. mRNA expression of metabolic genes associated with **e** gluconeogenesis, **f** cholesterol metabolism, **g** lipogenesis and lipolysis, and **h** adiponectin level as assessed by qPCR ($n = 6$). Data are presented as the mean ± SEM of six mice per group from three independent experiments. $^{*}P < 0.05$; $^{**}P < 0.01$; $^{***}P < 0.001$ vs. miR-scramble

Overexpression of miR-99a markedly diminished LPS/IFN-γ-induced macrophage bactericidal activity when compared to miR-scramble control (Fig. 2e).

miR-99a silencing experiments were performed with miR-99a or miR-scramble antagomir. BMDMs were infected with lentivirus containing miR-99a or miR-scramble antagomir, followed by stimulation with IL-4 for M2 phenotype activation. The inhibition of miR-99a was confirmed by qPCR (Fig. S1B). miR-99a antagomir treatment significantly inhibited the IL-4-induced increase in the mRNA expression of YM-1, ARG-1, and PPARγ when compared to scramble-treated control (Fig. 2f). Similar results were obtained at the protein level, with a significant decrease in CD206 expression after miR-99a antagomir treatment (Fig. 2g).

miR-99a mimics prevent M1 macrophage activation by targeting TNFα

To address the mechanism by which miR-99a affects macrophage phenotype activation, we performed in silico analysis of mRNA target prediction.[34] Of the six prediction algorithms, four (miRWalk, RNAhybrid, miRanda, and TargetScan) identified a miR-99a-putative target site within the 3′-untranslated regions (3′-UTR) of TNFα (Fig. 3a, b). TNFα is a known inducer of M1 phenotype activation.[35] Furthermore, overexpression of miR-99a in LPS/IFN-γ-stimulated BMDMs significantly reduced TNFα expression at both the mRNA and protein levels when compared to scramble miRNA control (Fig. 3c, d). To further ascertain the direct effect of miR-99a on TNFα, we performed a luciferase reporter assay, in which binding of miR-99a at the 3′-UTR of TNFα was monitored. miR-99a overexpression significantly attenuated TNFα 3′-UTR (~2.5-fold) luciferase activity when compared to miR-scramble control (Fig. 3e), indicating that miR-99a directly binds to the 3′-UTR of TNFα. Lentiviral-mediated knockdown of TNFα by shRNA (shTNF) significantly reduced LPS/IFN-γ-induced TNFα mRNA expression in the BMDMs when compared to scramble shRNA-treated cells (Fig. S1C). Knockdown of TNFα significantly reduced the mRNA expression of proinflammatory M1 macrophage signature genes (iNOS, MCP-1, and IL-1β) (Fig. S1D) and significantly increased the mRNA expression of M2 markers (YM-1, ARG-1, and PPARγ) (Fig. S1E) in LPS/IFN-γ-stimulated BMDMs when compared to scrambled shRNA control. Additionally, the bactericidal activity of LPS/IFN-γ-stimulated cells that were pretreated with TNFα-shRNA was significantly reduced when compared to scramble shRNA control (Fig. S1F).

miR-99a mimics reduce M1 macrophage phenotype and adipose tissue inflammation in diabetic mice

Since the macrophage phenotype affects adipose tissue inflammation and insulin resistance, miR-99a expression was evaluated in eWAT of control (*db/+*) and diabetic (*db/db*) mice. miR-99a expression was significantly reduced in eWAT

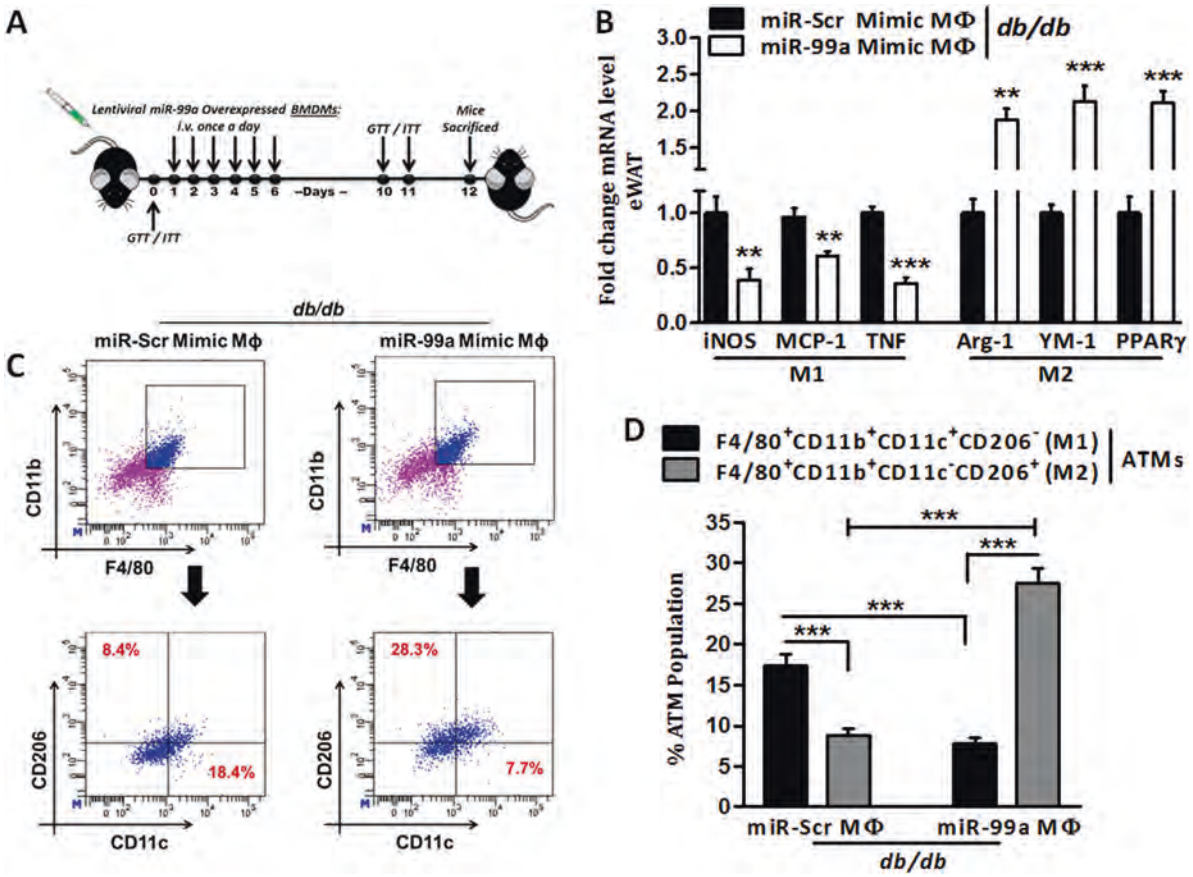

Fig. 8 miR-99a-overexpressed macrophages modulate ATM phenotype. **a** Treatment regime of miR-99a- or miR-scramble-overexpressed macrophages and timeline for the measurement of parameters. **b** *db/db* mice were treated with miR-99a- or miR-scramble-overexpressed macrophages, and mRNA expression of M1 (iNOS, MCP-1, and TNF) and M2 (YM-1, ARG-1, and PPARγ) macrophage signature genes was determined in total eWAT by qPCR ($n = 6$). **c** Dot plot represents labeling of F4/80$^+$CD11b$^+$CD11c$^+$CD206$^-$(M1) and F4/80$^+$CD11b$^+$CD11c$^-$CD206$^+$(M2) ATMs by flow cytometry in *db/db* mice treated with miR-99a- or miR-scramble-overexpressed macrophages ($n = 6$). **d** Quantification of figure **c**. Data are presented as the mean ± SEM of six mice per group from three independent experiments. $^{**}P < 0.01$; $^{***}P < 0.001$

(~2.5-fold) and F4/80$^+$sorted macrophages (~5-fold) from *db/db* mice when compared to *db/+* control mice (Fig. 4a, b). To further study the association of miR-99a with the macrophage phenotype in vivo, miR-99a expression was analyzed in F4/80$^+$CD11b$^+$CD11c$^+$CD206$^-$ M1 and F4/80$^+$CD11b$^+$CD11c$^-$CD206$^+$ M2-sorted ATMs from *db/+* animals. M2 ATMs from *db/+* mice showed a significantly increased expression of miR-99a when compared to M1 ATMs from *db/+* mice (Fig. 4c, d). On the basis of the decreased expression of miR-99a in ATMs from diabetic mice and its positive association with M2 ATMs, we hypothesized that miR-99a mimics may modulate the adipose tissue macrophage phenotype and inflammation. To confirm this, diabetic mice were treated with lentivirus containing miR-99a or miR-scramble mimics for three consecutive days (Fig. 4e). Overexpression of miR-99a was confirmed in the F4/80$^+$CD11b$^+$ ATMs and total eWAT (Fig. S2.A–C), as well as in F4/80$^+$CD11b$^+$ liver macrophages and total liver by qPCR (Fig. S2.D–F). Significantly upregulated mRNA expression of M2 and reduced M1 macrophage markers were found in total eWAT of miR-99a mimic-treated *db/db* mice when compared to miR-scramble-treated mice (Fig. 4f). To further assess the changes in macrophage phenotype, F4/80$^+$CD11b$^+$CD11c$^+$CD206$^-$M1 and F4/80$^+$CD11b$^+$CD11c$^-$CD206$^+$M2 ATMs from eWAT of *db/db* mice treated with miR-99a were quantified and evaluated by flow cytometry. miR-99a mimic-treated diabetic mice showed a significant increase in F4/80$^+$CD11b$^+$CD11c$^-$CD206$^+$ M2 ATMs and a decrease in F4/80$^+$CD11b$^+$CD11c$^+$CD206$^-$M1 ATMs when compared to miR-scramble-treated diabetic mice (Fig. 4g, h). Furthermore, eWAT of miR-99a-treated *db/db* mice showed a significant decrease in CD86 (Fig. 5a) and a significant increase in CD301 (Fig. 5b) staining when compared to miR-scramble-treated *db/db* mice. Moreover, in miR-99a-overexpressed *db/db* mice, there was a significant decrease in average adipocyte area when compared to miR-scramble-treated *db/db* mice (Fig. 5c). However, no significant difference in the number of F4/80$^+$Ly6c$^+$ ATMs was observed between the miR-99a- and miR-scramble-treated *db/db* mice (Fig. 5d).

miR-99a mimics improve systemic glucose homeostasis, insulin sensitivity, and dyslipidemia in diabetic mice

To assess whether miR-99a mimics also affect disease pathology, systemic glucose tolerance and insulin sensitivity were monitored in miR-scramble- or miR-99a-treated *db/db* mice (Fig. 6a–d). Administration of miR-99a in *db/db* mice significantly improved glucose tolerance ($p < 0.01$, Fig. 6a, b) and insulin sensitivity ($p < 0.01$, Fig. 6c, d) when compared to miR-scramble-treated *db/db* mice. The HOMA-IR index also decreased in miR-99a-treated *db/db* mice when compared to miR-scramble control (Fig. 6e). Moreover, random blood glucose levels were significantly lower in miR-99a-treated *db/db* mice than in miR-scramble control (Fig. S3A). At day 7, a significant decrease in the fasting glucose (Fig. S3B) and insulin levels (Fig. S3C) was observed in miR-99a-treated mice

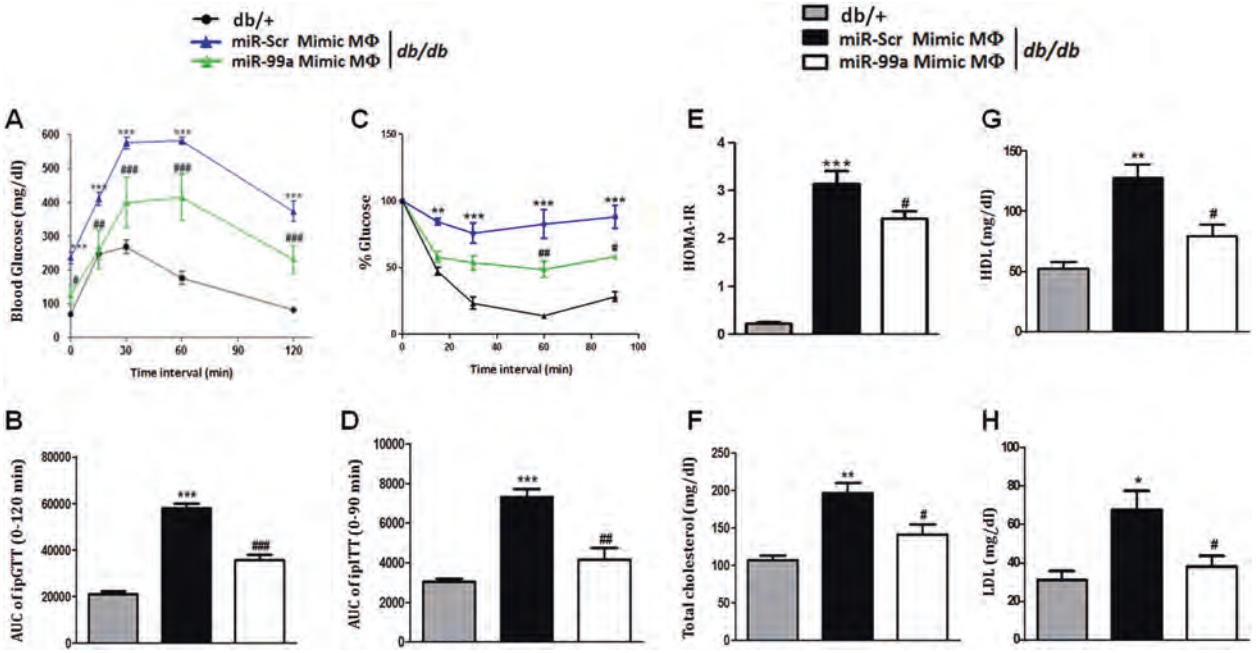

Fig. 9 miR-99a-overexpressed macrophages regulate systemic glucose, insulin tolerance, and lipid metabolism. Analysis was performed 4 days after the adoptive transfer of miR-99a- or miR-scramble-overexpressed macrophages. **a** Intraperitoneal glucose tolerance test (ipGTT), **b** the area under the curve (AUC) during ipGTT. **c** Insulin tolerance test (ITT). **d** The area under the curve (AUC) during ITT. **e** HOMA-IR. **f** Total cholesterol. **g** High-density lipoprotein (HDL). **h** Low-density lipoprotein (LDL). Data are presented as the mean ± SEM of 9–12 mice per group from three independent experiments. $^{*}P < 0.05$; $^{**}P < 0.01$; $^{***}P < 0.001$ *db/+* vs. miR-scramble macrophage-treated *db/db*, and $^{\#}P < 0.05$; $^{\#\#}P < 0.01$; $^{\#\#\#}P < 0.001$; miR-scramble- vs. miR-99a macrophage-treated *db/db*

when compared to miR-scramble control. To check the effect of miR-99a on lipid parameters, a plasma lipid profile was generated. It was shown that miR-99a induced a significant decrease in the circulatory total cholesterol, HDL-cholesterol, and LDL-cholesterol levels (Fig. 6f, h) when compared to miR-scramble-treated *db/db* mice. However, the circulatory triglyceride levels and body weight of *db/db* animals were unaffected by miR-99a treatment (Fig. S3D and E).

miR-99a mimics improve insulin signaling and regulate metabolism in diabetic mice

Inactivation of the insulin pathway is accompanied by an increased phosphorylation of IRS-1 at serine 307 (Ser-307)[36] and a decreased phosphorylation of Akt at serine 473 (Ser-473). miR-99a mimics significantly reduced the phosphorylation of IRS1 at Ser-307 (Fig. 7a, b) and concomitantly enhanced the phosphorylation of AKT at Ser-473 (Fig. 7c, d) in the eWAT and liver of *db/db* mice when compared to miR-scramble control. In the liver of miR-99a-treated mice, the mRNA expression of gluconeogenesis (PEPCK, G6PC, and FOXO1) and cholesterol metabolism-associated genes (SREBP1 and LXRα) was significantly downregulated when compared to miR-scramble-treated mice (Fig. 7e, f). Similarly, in the eWAT of miR-99a-treated *db/db* mice, a significant decrease in the mRNA expression of the lipolysis gene HSL (~2.5-fold) was observed when compared to miR-scramble-treated *db/db* mice (Fig. 7g). However, genes associated with lipogenesis (ACC1 and FAS) were unaffected (Fig. 7g). Additionally, miR-99a mimics significantly enhanced adiponectin levels (~2.5-fold) in the eWAT when compared to miR-scramble-treated *db/db* mice (Fig. 7h).

Adoptive transfer of miR-99a-overexpressed macrophages reduces the M1 macrophage phenotype and adipose tissue inflammation in diabetic mice

To assess the role of macrophage specific miR-99a effect on macrophage phenotype, adipose tissue inflammation, and insulin resistance, adoptive transfer experiments were performed. *db/db* mice were administered miR-99a- or miR-scramble-overexpressing macrophages for six consecutive days (Fig. 8a). The adoptive transfer of macrophages containing overexpressed miR-99a into *db/db* mice induced a significant increase in the mRNA expression of YM-1, ARG-1, and PPARγ genes, and a significant decrease in the mRNA expression of iNOS, MCP-1, and IL-1β genes in the eWAT when compared to miR-scramble (Fig. 8b), indicating M2 macrophage phenotype activation. To further assess macrophage phenotype changes, quantification of $F4/80^{+}CD11b^{+}CD11c^{+}CD206^{-}$(M1) and $F4/80^{+}CD11b^{+}CD11c^{-}CD206^{+}$(M2) ATMs from eWAT was assessed by flow cytometry. Adoptive transfer of macrophages containing overexpressed miR-99a to *db/db* mice induced a significant increase in the $F4/80^{+}CD11b^{+}CD11c^{-}CD206^{+}$(M2) cell population, while a significant decrease in the $F4/80^{+}CD11b^{+}CD11c^{+}CD206^{-}$(M1) ATMs was observed when compared to miR-scramble control (Fig. 8c, d).

Adoptive transfer of miR-99a-overexpressed macrophages improves systemic glucose tolerance, insulin sensitivity, and dyslipidemia in diabetic mice

To assess whether adoptive transfer of miR-99a-overexpressing macrophages also affects disease pathology, the systemic glucose tolerance and insulin sensitivity were monitored in diabetic mice treated with miR-99a- or miR-scramble-overexpressed macrophages (Fig. 9a–d). Delivery of miR-99a-overexpressed macrophages to *db/db* mice significantly improved the glucose tolerance ($p < 0.001$, Fig. 9a, b), insulin sensitivity ($p < 0.01$, Fig. 9c, d), HOMA-IR index ($p < 0.05$, Fig. 9e), and random glucose ($p < 0.01$, Fig. S4A) when compared to miR-scramble. A significant decrease in the fasting blood glucose ($p < 0.001$, Fig. S4B) and insulin levels ($p < 0.05$, Fig. S4C) was observed in *db/db* mice treated with miR-99a-overexpressing macrophages when compared to miR-scramble control. Additionally, a significant decrease in the circulatory total cholesterol ($p < 0.05$, Fig. 9f), HDL-cholesterol ($p < 0.05$, Fig. 9g), and LDL-cholesterol ($p < 0.05$, Fig. 9h) was observed in *db/db* mice treated with miR-99a-

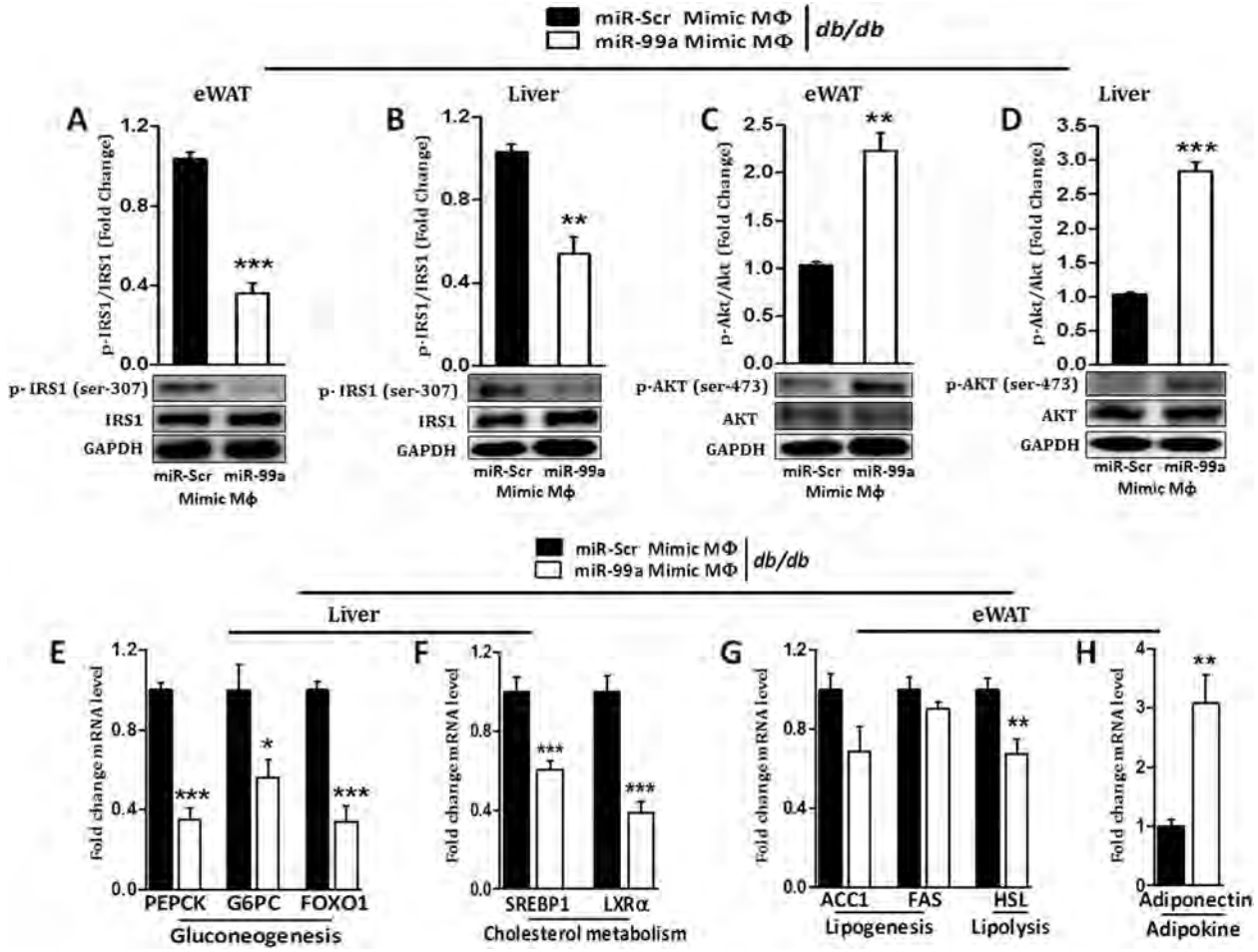

Fig. 10 miR-99a-overexpressed macrophages improve insulin signaling, glucose, and lipid metabolism in *db/db* mice. Adipose tissue and liver samples were collected from *db/db* mice treated with miR-99a- or miR-scramble-overexpressed macrophages, and western blotting was performed to detect the levels of **a** p-IRS-1 (Ser-307) and IRS-1 in eWAT. **b** p-IRS-1 (Ser-307) and IRS-1 in liver. **c** p-AKT (Ser-473) and AKT in eWAT. **d** p-AKT (Ser-473) and AKT in liver. Phosphorylation of IRS-1 and AKT was normalized to their respective total proteins. The bar diagram shows the quantification of the blots from at least three independent experiments. GAPDH was used as a loading control. mRNA expression of metabolic genes associated with **e** gluconeogenesis, **f** cholesterol metabolism, **g** lipogenesis and lipolysis, and **h** adiponectin levels, as assessed by qPCR ($n = 6$). Data are presented as the mean ± SEM of at least six mice per group from three independent experiments. $^{*}P < 0.05$; $^{**}P < 0.01$; $^{***}P < 0.001$ vs. miR-scramble macrophage

overexpressed macrophages when compared to miR-scramble control. However, circulating triglycerides and the body weight (Fig. S4.D and E) of *db/db* animals treated with miR-99a-overexpressing macrophages were unaffected when compared to miR-scramble control.

Adoptive transfer of miR-99a-overexpressed macrophages improves insulin signaling and regulates metabolism in diabetic mice

To evaluate the effect of miR-99a-overexpressing macrophages on insulin sensitivity, the insulin signaling cascade was assessed. Adoptive transfer of miR-99a-overexpressing macrophages in *db/db* mice significantly reduced the phosphorylation of IRS1 at Ser-307 (Fig. 10a, b) and enhanced AKT Ser-473 phosphorylation (Fig. 10c, d) in the eWAT and liver when compared to miR-scramble control. Hepatic mRNA expression of gluconeogenesis (PEPCK, G6PC, and FOXO1) and cholesterol metabolism-associated genes (SREBP1 and LXRα) was significantly downregulated in *db/db* mice that received miR-99a-overexpressing macrophages when compared to miR-scramble control (Fig. 10e, f). miR-99a-overexpressing macrophages induced a significant decrease in the eWAT mRNA expression of lipolysis gene HSL when compared to miR-scramble control (Fig. 10g). However, genes associated with lipogenesis (ACC1 and FAS) were unaffected (Fig. 10g). In the diabetic mice, miR-99a-overexpressing macrophages significantly enhanced adiponectin levels (~3-fold) in the eWAT when compared to miR-scramble control (Fig. 10h).

DISCUSSION

Several studies have established the importance of macrophages and their phenotype in the maintenance of metabolic homeostasis.[37] The present study demonstrates the role of miR-99a in M1 macrophage phenotype activation by targeting TNFα. miR-99a mimics regulate adipose tissue inflammation and insulin resistance. A differential expression pattern of miR-99a was observed during M1 and M2 macrophage phenotype activation by LPS/IFN-γ and IL-4, respectively. The enhanced expression of miR-99a in M2- (IL-4) and M1 (LPS/IFN-γ)-derived M2 macrophages suggests a role of this miRNA in preventing M1 phenotype activation. Since miR-99a mimics in LPS/IFN-γ-stimulated macrophages increased M2 and decreased M1 markers, it can be speculated that miR-99a can inhibit M1 phenotype activation. miR-99a mimics also diminished the bactericidal activity of LPS/IFN-γ-stimulated BMDMs (Fig. 2d), indicating an inhibition of M1 macrophage function. Furthermore, silencing of miR-99a by miR-99 antagomir

reduced the M2 phenotype, suggesting the specific role of this miRNA in M2 phenotype activation.

miRNAs act as a critical regulator of several biological processes by regulating the expression of their target genes.[38,39] Four of the six computational algorithms used in the present study identified the 3′-UTR of TNFα as a probable target site of miR-99a. A decrease in the TNFα expression in miR-99a-overexpressing and LPS/IFN-γ-stimulated BMDMs suggests that TNFα is a probable target of miR-99a in macrophages. Furthermore, the reduced luciferase activity of TNFα 3′-UTR in miR-99a-overexpressing cells confirmed that TNFα is a direct target of miR-99a. TNFα silencing in LPS/IFN-γ-stimulated BMDMs promoted the M2 phenotype, probably by reducing M1 phenotype activation since a decrease in mRNA expression of iNOS, MCP-1, and IL-1β was observed along with an enhanced expression of YM-1, ARG-1, and PPARγ. TNFα negatively regulates PPARγ expression and activity, which is a positive modulator of M2 phenotype activation.[40,41] Therefore, silencing TNFα in M1 macrophages may indirectly promote M2 phenotype activation. Furthermore, the reduced bactericidal activity observed in terms of enhanced CFU formation in TNFα-silenced and LPS/IFN-γ-stimulated BMDMs demonstrated the significance of TNFα in attenuating M1 macrophage function. It can therefore be speculated that in BMDMs, miR-99a modulates M1 phenotype activation and function by targeting TNFα.

Previous studies have revealed that under diabetic conditions, ATMs preferentially undergo proinflammatory M1 phenotype activation, which regulates adipose tissue inflammatory responses.[42] In concomitance with this notion, a reduced expression of miR-99a in eWAT and F4/80$^+$ ATMs of diabetic mice established an inverse relation between miR-99a expression and adipose tissue inflammation (Fig. 5a, b). This correlated with the in vitro findings in the BMDMs.

Moreover, phenotypic switching of ATMs into the alternatively activated M2 is sufficient to modulate adipose tissue function.[22,42,43] In the eWAT of diabetic mice, miR-99a mimics significantly attenuated F4/80$^+$CD11b$^+$CD11c$^+$CD206$^-$M1 and enhanced the F4/80$^+$CD11b$^+$CD11c$^-$CD206$^+$M2 macrophage populations, while significantly decreasing iNOS, MCP-1, and TNFα and significantly increasing ARG-1, YM-1, and PPARγ mRNA expression. In miR-99a-treated *db/db* mice, an attenuated CD86 and enhanced CD301 staining in eWAT again suggested the suppression of M1 macrophage and activation of the M2 phenotype. The beneficial effect of miR-99a mimics was also evident at the morphological level, since significant attenuation in adipocyte hypertrophy was observed when compared to miR-scramble mimics.

Macrophage recruitment in adipose tissue is a key feature of the diabetic condition.[22] However, the number of F4/80$^+$Ly6c$^+$ ATMs did not differ significantly between miR-99a- and miR-scramble-overexpressed diabetic mice, indicating that macrophage infiltration was unaffected.

The therapeutic potential of miR-99a in diabetic mice was evident due to an improved glucose tolerance and insulin sensitivity and the alleviation of hyperglycemia, hyperinsulinemia, and hyperlipidemia after miR-99a mimics were administered when compared to miR-scramble mimics.

Inflammatory stimuli such as TNFα inhibits the action of insulin by facilitating the inhibitory phosphorylation of insulin receptor substrate-1 (IRS1) on Ser-307 in the diabetic state.[36] Therefore, in the present study, it is quite possible that miR-99a improves insulin signaling by inhibiting TNFα. This hypothesis gains support from the observation that miR-99a mimics reduced inhibitory IRS-1 phosphorylation and induced hyperphosphorylation of AKT in the liver and eWAT when compared to miR-scramble control. In the adipose tissue, miR-99a mimics enhanced anti-inflammatory adiponectin, which may also complement M2 macrophage phenotype activation.

Impaired gluconeogenesis in the liver leads to hyperglycemia in type-2 diabetes.[44,45] In diabetic mice, miR-99a mimics significantly reduced the hepatic mRNA expression of genes involved in glucose (PEPCK, G6PC, and FOXO1) and cholesterol (SREBP1 and LXRα) metabolism, thereby explaining the beneficial effects of this therapy on circulatory glucose and cholesterol levels. In the adipose tissue, miR-99a mimics can also inhibit lipolysis, since a significant decrease in HSL mRNA expression was observed. However, lipogenesis seems to be unaffected, since mRNA expression of ACC1 and FAS was unaffected in miR-99a mice.

Adoptive transfer of miR-99a-overexpressed macrophages in diabetic animals established an essential role of macrophage specific miR-99a in the disease pathology. Adoptive transfer of miR-99a-overexpressed macrophages in diabetic animals promoted M2 phenotype activation and improved systemic glucose levels, insulin sensitivity, diabetes-associated dyslipidemia, and insulin signaling.

The present study demonstrates the role of miR-99a in preventing M1 macrophage phenotype activation and adipose tissue inflammation. Mechanistically, miR-99a targets TNFα and inhibits M1 macrophage phenotype and function. The present study also demonstrates the modulation of M1 macrophage phenotype activation as one of the possible mechanisms by which miR-99a mimics alleviate adipose tissue inflammation and insulin resistance. Our study speculates the therapeutic potential of miR-99a in diabetes-associated metabolic dysfunction.

ACKNOWLEDGEMENTS

The authors gratefully acknowledge the technical help provided by Mr. A.L. Vishwakarma and Mr. C.P. Pandey. This work was supported by the CSIR-Network project: "Towards a holistic understanding of complex diseases: Unraveling the threads of complex disease (THUNDER)". A.J. and M.M. are supported by UGC, New Delhi, P.M. is supported by CSIR, New Delhi, and S.S.R. is supported by THUNDER. CDRI Communication number: 9683

ADDITIONAL INFORMATION

Supplementary Information accompanies for this paper at https://doi.org/10.1038/s41423-018-0038-7.

Competing interests: The authors declare no competing interests.

REFERENCES

1. Han, M. S. et al. JNK expression by macrophages promotes obesity-induced insulin resistance and inflammation. *Science* **339**, 218–222 (2013).
2. Orr, J. S. et al. Toll-like receptor 4 deficiency promotes the alternative activation of adipose tissue macrophages. *Diabetes* **61**, 2718–2727 (2012).
3. Eguchi, J. et al. Interferon regulatory factor 4 regulates obesity-induced inflammation through regulation of adipose tissue macrophage polarization. *Diabetes* **62**, 3394–3403 (2013).
4. Odegaard, J. I. et al. Macrophage-specific PPARgamma controls alternative activation and improves insulin resistance. *Nature* **447**, 1116–1120 (2007).
5. Nishimura, S. et al. CD8+ effector T cells contribute to macrophage recruitment and adipose tissue inflammation in obesity. *Nat. Med.* **15**, 914–920 (2009).
6. Ji, Y. et al. Activation of natural killer T cells promotes M2 Macrophage polarization in adipose tissue and improves systemic glucose tolerance via interleukin-4 (IL-4)/STAT6 protein signaling axis in obesity. *J. Biol. Chem.* **287**, 13561–13571 (2012).
7. Scott, L. J. et al. A genome-wide association study of type 2 diabetes in Finns detects multiple susceptibility variants. *Science* **316**, 1341–1345 (2007).
8. O'Neill, L. A., Sheedy, F. J. & McCoy, C. E. MicroRNAs: the fine-tuners of Toll-like receptor signalling. *Nat. Rev. Immunol.* **11**, 163–175 (2011).
9. Zhuang, G. et al. A novel regulator of macrophage activation: miR-223 in obesity-associated adipose tissue inflammation. *Circulation* **125**, 2892–2903 (2012).
10. Yao, F. et al. Adipogenic miR-27a in adipose tissue upregulates macrophage activation via inhibiting PPARgamma of insulin resistance induced by high-fat diet-associated obesity. *Exp. Cell Res.* **355**, 105–112 (2017).
11. Rupaimoole, R. & Slack, F. J. MicroRNA therapeutics: towards a new era for the management of cancer and other diseases. *Nat. Rev. Drug Discov.* **16**, 203–222 (2017).

12. Sun, D. et al. miR-99 family of MicroRNAs suppresses the expression of prostate-specific antigen and prostate cancer cell proliferation. *Cancer Res.* **71**, 1313–1324 (2011).
13. Li, Q. et al. Overexpression of microRNA-99a attenuates cardiac hypertrophy. *PLOS One* **11**, e0148480 (2016).
14. Arner, P. & Kulyte, A. MicroRNA regulatory networks in human adipose tissue and obesity. *Nat. Rev. Endocrinol.* **11**, 276–288 (2015).
15. Heneghan, H. M., Miller, N., McAnena, O. J., O'Brien, T. & Kerin, M. J. Differential miRNA expression in omental adipose tissue and in the circulation of obese patients identifies novel metabolic biomarkers. *J. Clin. Endocrinol. Metab.* **96**, E846–E850 (2011).
16. Liao, B. et al. MicroRNA cluster 302–367 enhances somatic cell reprogramming by accelerating a mesenchymal-to-epithelial transition. *J. Biol. Chem.* **286**, 17359–17364 (2011).
17. Banerjee, S. et al. MicroRNA let-7c regulates macrophage polarization. *J. Immunol.* **190**, 6542–6549 (2013).
18. Kadl, A. et al. Identification of a novel macrophage phenotype that develops in response to atherogenic phospholipids via Nrf2. *Circ. Res.* **107**, 737–746 (2010).
19. Nasri, M., Karimi, A. & Allahbakhshian Farsani, M. Production, purification and titration of a lentivirus-based vector for gene delivery purposes. *Cytotechnology* **66**, 1031–1038 (2014).
20. Miller, M. R. & Blystone, S. D. Reliable and inexpensive expression of large, tagged, exogenous proteins in murine bone marrow-derived macrophages using a second generation lentiviral system. *J. Biol. Methods* **2**, e23 (2015).
21. Li, J. et al. Exosomes mediate the cell-to-cell transmission of IFN-alpha-induced antiviral activity. *Nat. Immunol.* **14**, 793–803 (2013).
22. Lumeng, C. N., Bodzin, J. L. & Saltiel, A. R. Obesity induces a phenotypic switch in adipose tissue macrophage polarization. *J. Clin. Invest.* **117**, 175–184 (2007).
23. Xiang, Y. et al. MicroRNA-487b is a negative regulator of macrophage activation by targeting IL-33 production. *J. Immunol.* **196**, 3421–3428 (2016).
24. Jain, M., Singh, A., Singh, V. & Barthwal, M. K. Involvement of interleukin-1 receptor-associated kinase-1 in vascular smooth muscle cell proliferation and neointimal formation after rat carotid injury. *Arterioscler. Thromb. Vasc. Biol.* **35**, 1445–1455 (2015).
25. Zheng, L. et al. Differential microRNA expression in human macrophages with mycobacterium tuberculosis infection of beijing/W and non-Beijing/W strain types. *PLOS One* **10**, e0126018 (2015).
26. Sun, X. et al. MicroRNA-181b improves glucose homeostasis and insulin sensitivity by regulating endothelial function in white adipose Tissue. *Circ. Res.* **118**, 810–821 (2016).
27. Tiwari, R. L. et al. PKCdelta-IRAK1 axis regulates oxidized LDL-induced IL-1beta production in monocytes. *J. Lipid Res.* **55**, 1226–1244 (2014).
28. Kaur, K. et al. Elevated hepatic miR-22-3p expression impairs gluconeogenesis by silencing the wnt-responsive transcription factor Tcf7. *Diabetes* **64**, 3659–3669 (2015).
29. Sun, X. J. et al. Deletion of interleukin 1 receptor-associated kinase 1 (Irak1) improves glucose tolerance primarily by increasing insulin sensitivity in skeletal muscle. *J. Biol. Chem.* **292**, 12339–12350 (2017).
30. Yokoyama, H. et al. Quantitative insulin sensitivity check index and the reciprocal index of homeostasis model assessment in normal range weight and moderately obese type 2 diabetic patients. *Diabetes Care* **26**, 2426–2432 (2003).
31. Ramkhelawon, B. et al. Netrin-1 promotes adipose tissue macrophage retention and insulin resistance in obesity. *Nat. Med.* **20**, 377–384 (2014).
32. Kanuri, B. N. et al. Altered glucose and lipid homeostasis in liver and adipose tissue pre-dispose inducible NOS knockout mice to insulin resistance. *Sci. Rep.* **7**, 41009 (2017).
33. Kanematsu, Y. et al. Critical roles of macrophages in the formation of intracranial aneurysm. *Stroke* **42**, 173–178 (2011).
34. Dweep, H., Sticht, C., Pandey, P. & Gretz, N. miRWalk—database: prediction of possible miRNA binding sites by "walking" the genes of three genomes. *J. Biomed. Inform.* **44**, 839–847 (2011).
35. Kroner, A. et al. TNF and increased intracellular iron alter macrophage polarization to a detrimental M1 phenotype in the injured spinal cord. *Neuron* **83**, 1098–1116 (2014).
36. Lavin, D. P., White, M. F. & Brazil, D. P. IRS proteins and diabetic complications. *Diabetologia* **59**, 2280–2291 (2016).
37. Liu, Y. C., Zou, X. B., Chai, Y. F. & Yao, Y. M. Macrophage polarization in inflammatory diseases. *Int. J. Biol. Sci.* **10**, 520–529 (2014).
38. Alvarez-Garcia, I. & Miska, E. A. MicroRNA functions in animal development and human disease. *Development* **132**, 4653–4662 (2005).
39. Rayner, K. J. et al. MiR-33 contributes to the regulation of cholesterol homeostasis. *Science* **328**, 1570–1573 (2010).
40. Ye, J. Regulation of PPARgamma function by TNF-alpha. *Biochem. Biophys. Res. Commun.* **374**, 405–408 (2008).
41. Zhang, B. et al. Negative regulation of peroxisome proliferator-activated receptor-gamma gene expression contributes to the antiadipogenic effects of tumor necrosis factor-alpha. *Mol. Endocrinol.* **10**, 1457–1466 (1996).
42. McNelis, J. C. & Olefsky, J. M. Macrophages, immunity, and metabolic disease. *Immunity* **41**, 36–48 (2014).
43. Zou J, et al. CD4+ T cells memorize obesity and promote weight regain. *Cell Mol. Immunol.* **14**, 1–10 (2017).
44. Basu, R., Chandramouli, V., Dicke, B., Landau, B. & Rizza, R. Obesity and type 2 diabetes impair insulin-induced suppression of glycogenolysis as well as gluconeogenesis. *Diabetes* **54**, 1942–1948 (2005).
45. Kabir, M. et al. Molecular evidence supporting the portal theory: a causative link between visceral adiposity and hepatic insulin resistance. *Am. J. Physiol. Endocrinol. Metab.* **288**, E454–E461 (2005).

Free Radical Biology and Medicine 168 (2021) 168–179

Contents lists available at ScienceDirect

Free Radical Biology and Medicine

journal homepage: www.elsevier.com/locate/freeradbiomed

Original article

Macrophage p47^{phox} regulates pressure overload-induced left ventricular remodeling by modulating IL-4/STAT6/PPARγ signaling

Sukka Santosh Reddy [a,b], Heena Agarwal [a,b], Anant Jaiswal [a], Kumaravelu Jagavelu [a,b], Madhu Dikshit [a,b,1], Manoj Kumar Barthwal [a,b,*]

[a] Pharmacology Division, CSIR-Central Drug Research Institute, Lucknow, 226031, India
[b] Academy of Scientific and Innovative Research (AcSIR), Ghaziabad, 201002, India

ARTICLE INFO

Keywords:
p47^{phox}
Macrophages
Angiotensin II
Hypertension
Hypertrophy
Fibrosis

ABSTRACT

NADPH oxidase (Nox) mediates ROS production and contributes to cardiac remodeling. However, macrophage p47^{phox}, a Nox subunit regulating cardiac remodeling, is unclear. We aimed to investigate the role of macrophage p47^{phox} in hypertensive cardiac remodeling. Pressure-overload induced by Angiotensin II (AngII) for two weeks in young adult male p47^{phox} deficient (KO) mice showed aggravated cardiac dysfunction and hypertrophy as indicated from echocardiographic and histological studies in comparison with wild-type littermates (WT). Additionally, LV of AngII-infused KO mice showed augmented interstitial fibrosis, collagen deposition and, myofibroblasts compared to AngII-infused WT mice. Moreover, these changes in AngII-infused KO mice correlated well with the gene analysis of hypertrophic and fibrotic markers. Similar results were also found in the transverse aortic constriction model. Further, AngII-infused KO mice showed elevated circulating immunokines and increased LV leukocytes infiltration and CD206^{+} macrophages compared to AngII-infused WT mice. Likewise, LV of AngII-infused KO mice showed upregulated mRNA expression of anti-inflammatory/pro-fibrotic M2 macrophage markers (Ym1, Arg-1) compared to AngII-infused WT mice. AngII and IL-4 treated bone marrow-derived macrophages (BMDMs) from KO mice showed upregulated M2 macrophage markers and STAT6 phosphorylation (Y641) compared to AngII and IL-4 treated WT BMDMs. These alterations were at least partly mediated by macrophage as bone marrow transplantation from KO mice into WT mice aggravated cardiac remodeling. Mechanistically, AngII-infused KO mice showed hyperactivated IL-4/STAT6/PPARγ signaling and downregulated SOCS3 expression compared to AngII-infused WT mice. Our studies show that macrophage p47^{phox} limits anti-inflammatory signaling and extracellular matrix remodeling in response to pressure-overload.

1. Introduction

Hypertensive cardiac remodeling is a significant risk factor for cardiovascular disease (CVD) and a primary reason for chronic heart failure. It is often characterized by left ventricular (LV) hypertrophy and cardiac fibrosis [1]. At the same time hypertrophic response is to maintain the cardiac function for a definite period. However, prolonged hypertrophy might be detrimental, thereby leading to cardiac dysfunction and sudden death [2]. The renin–angiotensin system (RAS) mediates cardiac adaptations to hemodynamic overload [3]. Angiotensin II, the major effector in the RAS, is shown to be involved in the development of cardiomyocyte hypertrophy and extracellular matrix (ECM) remodeling [4,5].

Recent studies show the causative role of the immune system in hypertrophy and heart failure [6]. Moreover, several findings have demonstrated the importance of infiltrating inflammatory cells such as macrophages during cardiac remodeling [6,7]. As major regulators of inflammation, macrophages, are highly resilient and can differentiate into M1 (pro-inflammatory) or M2 (anti-inflammatory/pro-fibrotic) macrophages. Lipopolysaccharide (LPS) or T-helper (Th) 1–produced interferon-γ (IFN- γ) induced M1 macrophages are associated with inflammation and tissue destruction. In contrast, Th2-produced interleukin-4 (IL-4) and IL-13 induced M2 macrophages show an anti-inflammatory phenotype associated with inflammation resolution and tissue healing. Hence, the Th1/2 response plays a critical regulatory role in maintaining pro- and anti-inflammatory macrophage balance

* Corresponding author. CSIR-Central Drug Research Institute, B.S. 10/1, Sector 10, Jankipuram Extension, Sitapur Road, Lucknow, 226031, India.
E-mail address: manojbarthwal@cdri.res.in (M.K. Barthwal).
[1] Present address: Translational Health Science and Technology Institute, Faridabad 121,001, Haryana, India.

https://doi.org/10.1016/j.freeradbiomed.2021.03.007
Received 7 December 2020; Received in revised form 2 March 2021; Accepted 5 March 2021
Available online 15 March 2021

[8]. IL-4 and IL-13-stimulated macrophages promote STAT6 activation, which is essential for anti-inflammatory macrophage polarization. Besides, peroxisome proliferator-activated receptors (PPARγ and PPARδ) activation is crucial for implementing the M2 macrophage program. Importantly, Arginase-1 mRNA expression and activity, which promotes tissue repair, is a hallmark of M2 macrophages. Moreover, the M2 program is linked with the upregulation of C-type lectins, mannose receptor (CD206), chitinase family proteins, resistin-like molecules, and IL-10, thus contributing to immunomodulatory function [9]. Likewise, Kruppel-like factor 4 (KLF4) mediated IL-4 induced M2 polarization leads to an increased propensity towards anti-inflammatory milieu [10]. Besides, suppressors of cytokine signaling (SOCS) proteins, CIS and SOCS1–7, negatively regulates Janus kinase (JAK)–signal transducer and activator of transcription (STAT) signaling pathway through a variety of mechanisms, thereby modulating both innate and adaptive immune responses [11].

Nicotinamide adenine dinucleotide phosphate (NADPH) oxidases (Nox) are the enzymes involved in the superoxide production via molecular oxygen. Nox2 is present in endothelial cells, vascular smooth muscle cells, adventitial fibroblasts, and cardiomyocytes. Phosphorylation of $p47^{phox}$ initiates assembly and activation of Nox2 by various kinases. Correspondingly, Nox activation and elevated oxidative stress play a key role in experimental and human heart failure. Deleting $p47^{phox}$ has been shown to attenuate myocardial infarction (MI)–induced ventricular remodeling and progression of diabetic nephropathy and suppress angiotensin II-induced superoxide generation in the cardiovascular system [12]. In contrast, deficiency of the $p47^{phox}$ has also been shown to contribute to elevated blood pressure in a ROS-independent manner and increased susceptibility to biomechanical stress and heart failure [12,13]. However, the role of macrophage $p47^{phox}$ in mediating cardiac hypertrophy and fibrosis under the setting of hypertension is still not clear.

Accordingly, we hypothesized that macrophage $p47^{phox}$ could play a vital role in pressure-overload induced cardiac hypertrophy and dysfunction via regulating pro- and anti-inflammatory balance, macrophage infiltration, and their propensity to modulate the extracellular matrix remodeling.

2. Materials & methods

2.1. Chemicals & antibodies

RevertAid H Minus first strand cDNA synthesis kit (Fermentas Life Sciences, Vilnius, Lithuania), 2X Maxima SYBR Green RT-PCR Master Mix (Roche Applied Science, Lewes, UK) and all the primers used for qPCR studies were purchased (Integrated DNA technology, India). Primary antibodies were purchased against CD86, STAT1, p-STAT1, IRF4 and OPN1 (Santa Cruz, CA); STAT3, p-STAT3, PPARγ, SOCS3 and KLF4 and GAPDH (Cell Signaling Technology, Danvers, MA, USA); α-SMA (Sigma Aldrich Co., St. Louis, USA); while those against Collagen1, CD206, CD45, TGF-β1, Mac3 and Ki67 (Abcam, UK). Except Angiotensin II (Merck, USA), all the other fine chemicals including secondary antibody against β-Actin were procured from Sigma Aldrich Co., St. Louis, USA).

2.2. Cell culture and treatments

BMDMs were isolated from the femur and tibia of WT or KO mice. In brief, the bones were flushed with ice-cold PBS containing 20 U/ml heparin and later incubated with sterile 0.843% ammonium chloride solution for approximately 10 min for erythrocytes lysis. Further, a single-cell suspension was obtained by straining through cell strainer (70-μm). The cells were then plated in RPMI medium (Sigma Aldrich Co., St. Louis, USA) supplemented with FBS (10%, Gibco) and MCSF (10 ng/ml, Peprotech, USA) for 7 days. On the seventh day, cells were starved from MCSF for 12hr and treated with AngII (1 μM, Calbiochem, USA) and/or IL-4 (20 ng/ml, Peprotech, USA) for 24hr and analysed further [14].

2.3. Animals and pressure overload model

Male 8–10 weeks old $p47^{phox}$ knockout [B6 (Cg)-$Ncf1^{m1J}$/J, stock no.004742, genetic background C57BL/6 J; hereinafter referred to as KO or $p47^{-/-}$] were procured from the Jackson Laboratory (Bar Harbor, ME) and maintained in specific pathogen-reduced conditions in individually ventilated cages with controlled temperature (25 ± 1 °C) and humidity (45–50%) with 12-h light/12-h dark cycle in the CDRI animal house facility, National Laboratory Animal Center (NLAC). The knockout mice were confirmed by genotyping where tail clips were digested using lysis buffer and proteinase K at 65° and genomic DNA was isolated using (Qiagen Kit, Cat. 158,267) and PCR was run using conventional protocol and Ncf1 primers (Table S1) provided by JAX labs as described previously [15,16] and the appearance of 102 bp and 58 bp shows that these mice are homozygous mutants (Figure S15) besides western blotting at indicated time points (Figure S16). Age and body weight-matched wild-type C57BL/6 J littermates (WT) were served as controls. Animals received autoclaved standard chow diet and water *ad libitum* containing antibiotics (Co-trimoxazole; 30 mg/kg). All experimental protocols are approved by our institutional Ethical Committee (IAEC/2018/F-54) following the guidelines of CPCSEA (Committee for the Purpose of Control and Supervision of Experiments on Animals) which complies with International norms of INSA (Indian National Science Academy). To maintain model consistency [17] and avoid hormonal interference, male mice were preferred over female.

To induce cardiac hypertrophy, mice were anaesthetised with the intraperitoneal injection of ketamine (80 mg/kg) and xylazine (15 mg/kg) mixture [18] and implanted subcutaneously with osmotic minipumps (ALZET Model 2002, DURECT, Cupertino, CA) for 14 days containing saline (vehicle) or a pressor dose of AngII (1500 ng/kg/min) [19]. In another model of pressure overload-induced LVH, minimally invasive transverse aortic constriction (mTAC) was performed on WT and KO mice as described previously [20]. Briefly, mice were anaesthetised and subjected to limited median sternotomy under a surgical microscope. A nylon suture (7–0) was placed around the aorta and the needle between the innominate and the left common carotid artery and suture was tied against the blunt needle and promptly removed thereafter. The sham surgery involved all the above procedure except that the aorta was not constricted. After the study period, mice were euthanized by cardiac blood collection under anaesthesia [8], and the LV was perfused with PBS. The hearts were removed and prepared for further histological and molecular analyses.

2.4. Enzyme-linked immunosorbent assay (ELISA) & multiplex analysis

IL-4 concentration in plasma samples were determined using ELISA kit (BD OptEIA™ set, BD Biosciences, San Diego, USA) and the levels of various immunokines (20-plex) were measured using multiplex bead array based on Luminex xMAP technology (USA), as previously described [21].

2.5. Echocardiographic analysis & blood pressure measurement

Echocardiography was performed using a Vevo 1100 high-resolution ultrasound imaging system (VisualSonics Inc., Toronto, Canada) with an MS400 scan head (30 MHz) after anaesthesia as previously described [18]. Briefly, the LV internal diameter (LVID) and anterior and posterior wall thickness (LVAW and LVPW) were measured using M-mode tracings over 3 consecutive cardiac cycles using Vevo® LAB software version 1.7.1 from the parasternal long-axis view (PSLA) of the heart. At the papillary muscles level, the probe was placed to obtain the parasternal short-axis view (PSSA/SAX) heart images.

Tail-cuff method (NIBP-8, Columbus Instruments, USA) was used to

measure blood pressure changes as previously described [19].

2.6. RNA isolation and real-time PCR

Total RNA from LV tissue of different groups was extracted by using TRIzol reagent (Takara Bio, Japan) as described previously [19]. The cDNA was amplified in PCRs by using different primers (Table S1). Samples were incubated at 95 °C for 5 min, followed by 45 cycles, each cycle consisting of denaturation at 95 °C for 15s and annealing at 59 °C for 20s and extension at 72 °C for 15s. Comparative cycle threshold ($2^{-\Delta\Delta Ct}$) method was used for relative quantification. All data were normalized to 18S to calculate the relative expression.

2.7. Protein extraction and western blot analysis

BMDMs or LV tissue from mice was lysed in lysis buffer (Table S2) and extracts were collected after centrifugation (13,000×*g*, 10 min) and BCA reagent was used to determine the protein concentration. Then, the protein was separated on 8–12% SDS-PAGE and transferred to PVDF membrane. Later, the membrane was blocked with 5% BSA (in TBST) and probed with primary antibodies against various proteins of interest (STAT1, STAT3, STAT6, PPARγ, SOCS3, IRF4, OPN1 and KLF4) (Table S3). The specific protein bands were visualized by enhanced-chemiluminescence [19]. The densitometry values were normalized to that of total protein or loading control and the value is presented as a fold change.

2.8. Macrophage depletion and adoptive transfer of CFDA-SE labelled macrophages into mice

BMDMs were isolated from WT or KO mice and served as donor cells for transfer into saline- or AngII-infused WT or KO mice. For selective depletion of monocytes/macrophages, each WT or KO mouse were intraperitoneally injected with 200 μl of clodronate (Liposoma B.V, Science Park Amsterdam, The Netherlands) [22] as indicated in the schematic experimental timeline (Fig. 6A). Further, BMDMs from WT or KO mice were isolated and cultured, and then 2×10^6 CFDA-SE (carboxyfluorescein diacetate succinimidyl ester) labelled macrophages in 200 μl PBS were adoptively transferred into macrophage depleted WT or KO mice by intravenous injection, which were infused with saline or AngII as described previously [23].

2.9. Histopathology and immunostaining

Hematoxylin and eosin (H&E) staining were performed on paraffin-embedded sections for determining various immune cells infiltration and morphology. The interstitial fibrotic deposition was monitored on Masson Trichome (Sigma-Aldrich Co., St. Louis, USA) stained sections and Picrosirius red (Sigma-Aldrich Co., St. Louis, USA) staining was used to identify the collagen type (thick or thin fibres) deposition. Cardiac sections (5 μm) were stained with of FITC-conjugated wheat germ agglutinin (WGA) to assess cardiomyocyte cross-sectional area (CSA) by measuring at least 200 cells per slide. Immunohistochemistry (IHC) was performed with primary antibodies (CD45, Mac3, Ki67, TGF-β1, α-SMA and collagen1). Cardiac sections (7 μm) were incubated with the primary antibodies for CD86 and CD206 at 4 °C overnight and then with Alexa Fluor–conjugated (Invitrogen) secondary antibodies at room temperature for 2hr. Nuclei were stained by DAPI (Sigma-Aldrich Co., St. Louis, USA). Sections were viewed under Leica DM 5000 or DM 6000 fluorescent microscope (Wetzlar, Germany). The positive area or cell number of various infiltrated cells in the LV sections was determined by measuring in five randomly selected fields of view for each tissue section using a 20 × objective. ImageJ software (NIH, Bethesda, MD, USA) was used for the cell count from different fields [19].

2.10. Statistical analysis

All statistical analyses were performed with the GraphPad Prism 8.0 software (GraphPad Inc., La Jolla, CA, USA). Results were expressed as the mean ± standard error (S.E.). The statistical difference between groups was determined by one-way ANOVA followed by Bonferroni Post-Hoc test and probability value less than 0.05 was considered statistically different. Unpaired two tailed student t-test was used for differences between two groups.

3. Results

3.1. Loss of $p47^{phox}$ is associated with augmented left ventricular hypertrophy in angiotensin II-infused mice

Animals were subjected to various experimental procedures as indicated in the schematic timeline (Fig. 1A). No significant difference between WT and KO mice was observed in the basal LV dimensions and function, measured by echocardiography (Figure S1A). Though, saline-infused KO mice showed increased LVAW thickness compared to saline-infused WT mice (Figure S1A and Table S3). Angiotensin II infusion in WT and KO mice showed significant alterations in LV biometric (LVPW, LVAW, LVID and LV_{mass}) parameters compared to respective controls, which was further enhanced in KO mice (Figure S1A and Table S3). Importantly, EF% and HR did not differ between the genotypes after AngII infusion compared to respective controls (Table S3). Saline infused- KO mice showed slightly elevated basal SBP compared to WT mice, although statistically insignificant (103.9 ± 5.60 mmHg vs. 123 ± 6.73 mmHg) (Table S3). Both AngII-infused WT and KO mice showed significant elevation in SBP compared to respective controls, which was further augmented in KO mice (Table S3). Besides, both AngII-infused WT and KO mice showed a significant increase in HW/BW and HW/TL ratio, heart size, and LV cardiomyocyte CSA compared to respective controls that were further enhanced in KO mice (Table S3, Fig. 1B, and Figure S2A-S2B). Likewise, both AngII-infused WT and KO mice also showed upregulated fetal cardiac gene markers (Nppa, Nppb, Acta 1, Myh6 and Myh7) compared to respective controls (Figure S2C-S2G), with LV of AngII-infused KO showing highly upregulated fetal cardiac gene markers compared to AngII-infused WT mice (Figure S2C-S2G). Consistent with the data from AngII–treated mice, TAC-induced KO mice also showed augmented cardiac hypertrophic response compared to TAC-induced WT mice (Supplementary material: Page 11, Figures S6). Thus, $p47^{phox}$ deletion might accelerate AngII–induced pathological cardiac hypertrophy in mice.

3.2. Loss of $p47^{phox}$ is associated with aggravated cardiac fibrosis in angiotensin II-infused mice

To investigate the role of $p47^{phox}$ on cardiac fibrosis, harvested hearts were examined for fibrotic remodeling. We found that both AngII-infused WT and KO mice showed increased interstitial fibrotic and thick collagen fibres (Type I) deposition in the LV compared to respective controls that was further enhanced in KO mice (Fig. 1C and 1F and S3A-S3B). Immunohistochemistry revealed that both AngII-infused WT and KO mice showed increased expression of α-SMA, collagen 1 and TGF-β1 protein in the LV compared to respective controls that were further upregulated in KO mice (Figure S3A and S3C-S3E). Accordingly, both AngII-infused WT and KO mice also showed upregulated expression of fibrotic gene transcripts (α-SMA, Col1a2, Col3a1, TGF-β1 and TIMP1) in the LV compared to respective controls that were further upregulated in KO mice (Figure S4A-S4E). In line with the AngII model, TAC-induced KO mice also showed worsened cardiac fibrosis compared to TAC-induced WT mice (Figure S7A-S7F). Thus, the above findings indicate the regulatory role of $p47^{phox}$ in ECM remodeling under the setting of hypertension.

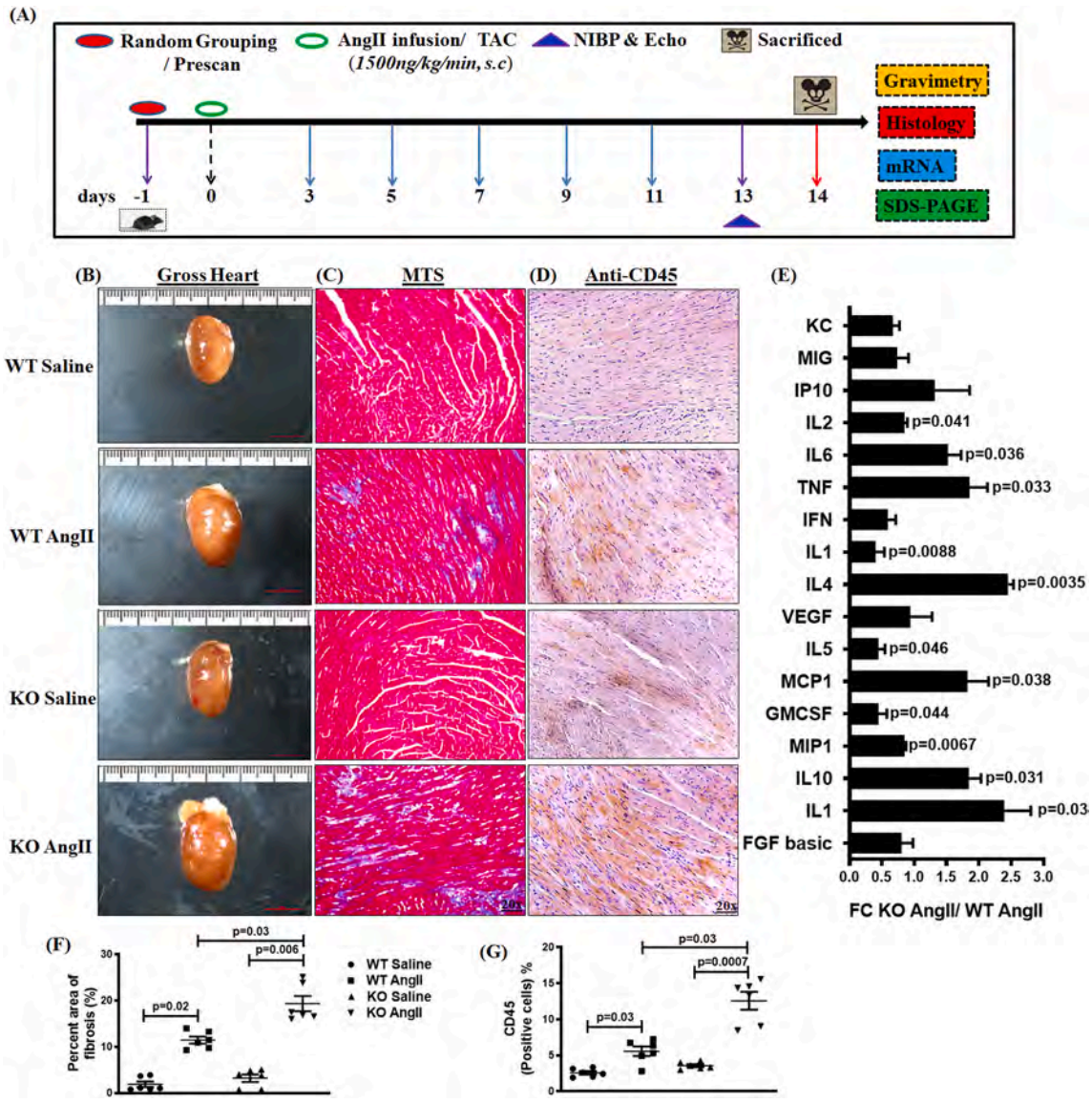

Fig. 1. Angiotensin II infusion in p47^{phox} KO mice is associated with enhanced cardiac remodeling. (A) Schematic representation of work plan. (B) Heart gross morphology. (C) Masson Trichome staining (MTS) of the LV. (D) Immunohistochemistry of CD45 in the LV. (E) Immunokines multiplexing. (F–G) Quantification of representative images as shown in panel (C) and (D). Data were expressed as mean ± SEM, n = at least 5 per group (except E, n= >10 per group). Total magnification ×200. Scale bar 50 μm. FC: fold change.

3.3. Loss of p47^{phox} is associated with pro- and anti-inflammatory imbalance in angiotensin II-infused mice

Based on the above findings that AngII-infused KO mice show altered cardiac biometrics and ECM remodeling, circulating levels of various immunokines were also investigated. Remarkably, AngII-infused KO mice showed prominent changes in the systemic levels of TH1/TH2 related cytokines and chemokines compared to AngII-infused WT mice (Fig. 1E). Further, both AngII-infused WT and KO mice showed increased infiltration of proinflammatory cells compared to respective controls that was further enhanced in KO mice (Figure S3A). Similarly, immunohistochemical staining of cardiac sections demonstrated the expression of CD45$^+$ and Mac3$^+$ markedly higher in KO than WT left ventricle after AngII infusion (Figs. 1D, 1G and 2A-2B). Further, both AngII-infused WT and KO mice also showed increased proliferation in the LV sections as indicated by increased Ki67$^+$ cells compared to respective controls that was significantly greater in KO mice (Fig. 2A and 2C). Also, LV infiltrated macrophages were further characterized for pro- and anti-inflammatory subsets using CD86$^+$ (M1 subtype) and CD206$^+$ (M2 subtype) markers respectively. We found that both AngII-infused WT and KO mice showed increased CD86$^+$ macrophages in the LV compared to respective controls with no significant difference between the genotypes (Fig. 2A and 2D). Notably, saline-infused KO mice showed elevated CD206$^+$ macrophages compared to saline-infused WT mice (Fig. 2A and 2E). Similarly, both AngII-infused WT and KO mice also showed increased CD206$^+$ macrophages in the LV compared to respective controls that was further enhanced in the KO mice (Fig. 2A and 2E). To substantiate the above findings, M1 (CD86, iNOS and CCR7) and M2 (CD206, YM1 and Arg1) macrophage gene markers were analysed in the LV of AngII-infused WT mice and found to be significantly altered compared to saline-infused WT mice (Figure S5A-S5C and S5D respectively), with a tendency of increase in YM1 and Arg1 expression (Figure S5E-S5F). Further, AngII-infused KO mice also showed significant increase in M1 and M2 gene markers compared to saline-infused KO mice (Figure S5A and S5D-S5F respectively), with a tendency of increase in iNOS and CCR7 expression (Figure S5B-S5C). However, AngII-infused KO mice showed downregulated M1 gene markers except for CD86 and upregulated M2 gene markers compared to AngII-infused WT mice

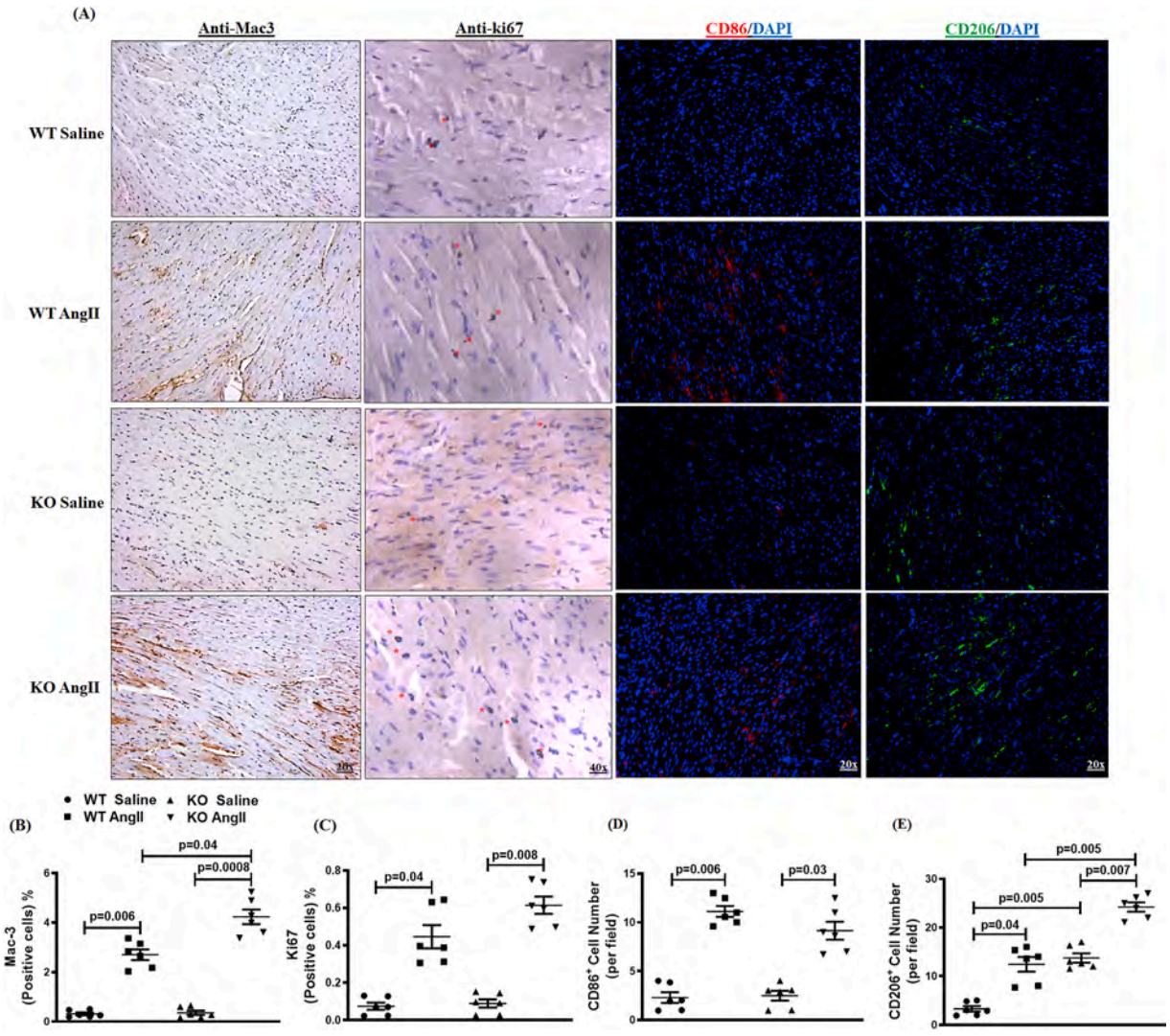

Fig. 2. Angiotensin II infusion in p47^{phox} KO mice leads to increased cardiac inflammation and macrophage infiltration. (A) Left to Right: Representative photomicrograph of immunohistochemical analysis (anti-Mac3 and anti-ki67) and immunofluorescence analysis (anti-CD86 and anti-CD206) in left ventricle of different groups. (B–E) Quantification of images as shown in panel (A). DAPI was used for nuclear staining. Data were expressed as mean ± SEM, n = at least 5 per group. Total magnification: ×200 (except ki67: X400). Scale bar: 50 μm (except ki67: 25 μm).

(Figure S5B-S5C and S5D-S5F respectively). These findings indicate that p47^{phox} deficiency is associated with altered systemic immunokine balance and increased anti-inflammatory milieu in the LV and thereby, affecting the pressure-overload induced cardiac remodeling process.

3.4. Angiotensin II and IL-4 treated p47^{phox} knock out macrophages shows augmented STAT6 phosphorylation

Since robust increase in IL-4 levels was observed in the present study and also it is well known that AngII mediates its pro-fibrotic role via elevated IL-4[24]. Therefore, to assess the mechanism *in vitro*, BMDMs isolated from WT and KO mice were treated with AngII and IL-4. Importantly, we found that both AngII and IL-4 treated WT and p47^{phox} KO macrophages showed upregulated pro-inflammatory/M1 macrophage gene markers (iNOS and IL-6) compared to respective controls (Fig. 3A and S8A). However, AngII and IL-4 treated WT macrophages showed greater expression of iNOS mRNA than AngII and IL-4 treated p47^{phox} KO macrophages (Fig. 3A). No significant change in mRNA expression of CD86 (Fig. 3B) and CCR7 (data not shown) was observed among the groups. Similarly, both AngII and IL-4 treated WT and p47^{phox} KO macrophages showed upregulated anti-inflammatory/M2 macrophage gene markers (IL-4 and YM1) compared to respective controls (Fig. 3C–3D). Interestingly, both AngII and IL-4 treated p47^{phox} KO macrophages also showed upregulated Arg1 and CD206 gene expression compared to untreated KO macrophages (Fig. 3E and S8B). Notably, both AngII and IL-4 treated p47^{phox} KO macrophages showed more robust upregulation of IL-4, YM1, Arg1 and CD206 genes compared to both AngII and IL-4 treated WT macrophages (Fig. 3C–3E and S8B). Further, both AngII and IL-4 treated p47^{phox} KO macrophages also showed upregulated fibrotic genes (Col1a2, Col3a1 and MMP-9) expression compared to untreated KO macrophages (Figure S8C-S8E). However, both AngII and IL-4 treated WT macrophages showed no significant change in Col1a2 and Col3a1 mRNA expression except MMP-9 ($p < 0.05$) compared to untreated WT macrophages (Figure S8C-S8E). Similar to M2/anti-inflammatory gene expression data, both AngII and IL-4 stimulation in KO macrophages showed highly upregulated Col1a2, Col3a1 and MMP-9 mRNA expression compared to both AngII and IL-4 stimulated WT macrophages (Figure S8C-S8E). Likewise, both AngII and IL-4 stimulated WT macrophages also showed a significant increase in STAT1 and PPARγ mRNA expression compared to untreated WT macrophages (Fig. 3F and 3H). However, both AngII and IL-4 stimulated WT macrophages showed no significant increase in STAT3 and STAT6

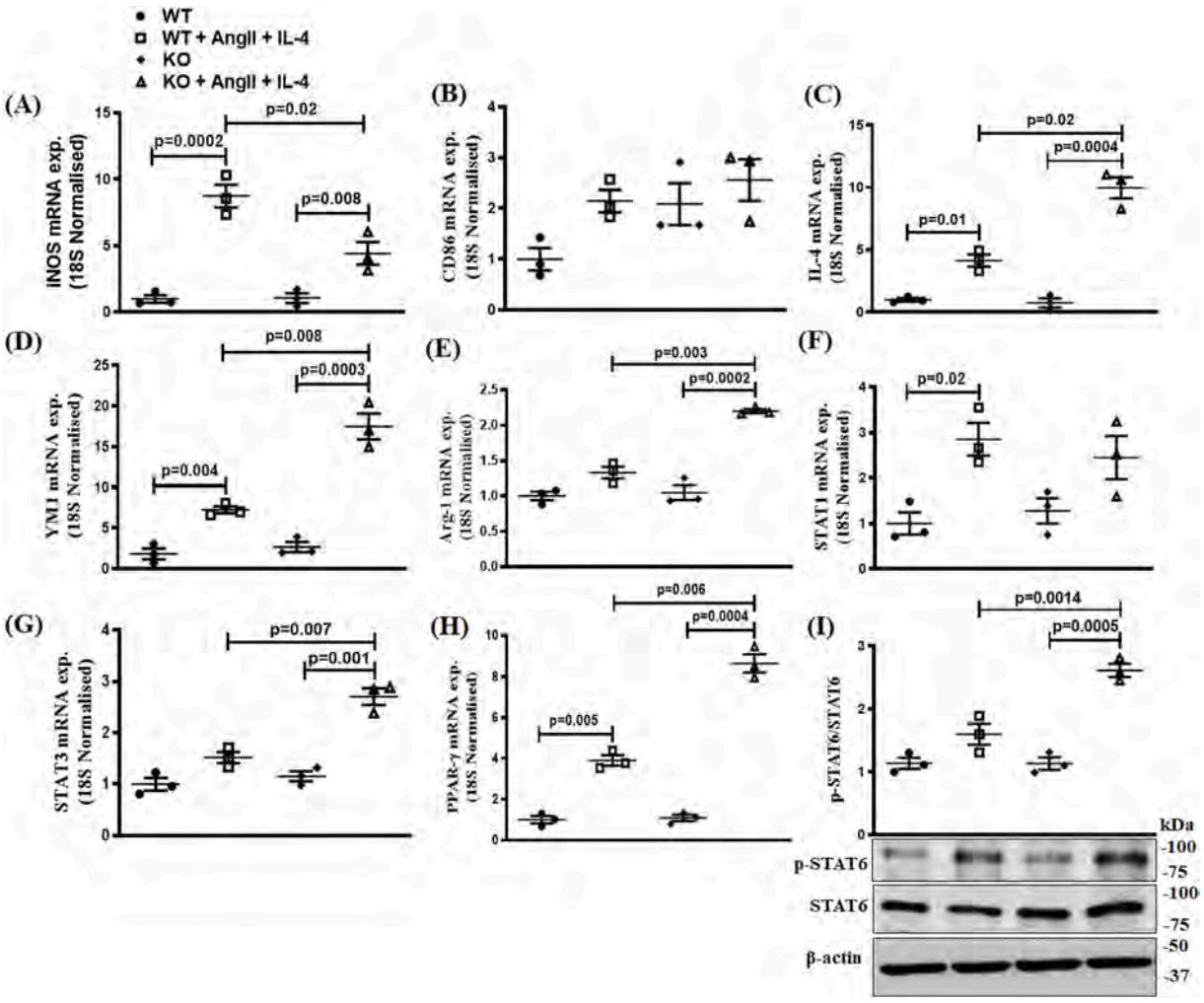

Fig. 3. Angiotensin II and IL-4 treatment in p47^{phox} KO mice BMDMs shows increased phosphorylation of STAT6. (A–H) Relative mRNA expression of iNOS (A), CD86 (B), IL-4 (C), YM1 (D), Arg-1 (E), STAT1 (F), STAT3 (G) and PPAR-γ (H) by Real-time PCR. 18S was used as a loading control. (I) Western blot images and quantification of STAT6 in cell lysates. β-actin was used as loading control. Data were expressed as mean ± SEM from three independent experiments. The blots are representatives of three similar experiments.

mRNA expression compared to untreated WT macrophages (Fig. 3G and S8F). Yet, both AngII and IL-4 stimulated KO macrophages showed a significant increase in STAT3, STAT6 and PPARγ (Fig. 3G, S8F and 3H) and no change in STAT1 (Fig. 3F) mRNA expression compared to untreated KO macrophages. Remarkably, both AngII and IL-4 stimulated KO macrophages showed highly upregulated expression of STAT3, STAT6 and PPARγ mRNA compared to both AngII and IL-4 stimulated WT macrophages (Fig. 3G, S8F and 3H). We next observed for the modifications in STAT6 protein phosphorylation (Y641) indicating STAT6 activation [25]. We found that both AngII and IL-4 stimulated KO macrophages showed a significant increase in STAT6 phosphorylation compared to untreated KO macrophages (Fig. 3I). However, both AngII and IL-4 stimulated WT macrophages showed no significant change in STAT6 phosphorylation compared to untreated WT macrophages (Fig. 3I). Interestingly, both AngII and IL-4 stimulated KO macrophages showed enhanced p-STAT6 protein expression compared to both AngII and IL-4 stimulated WT macrophages (Fig. 3I). These findings indicate that AngII and IL-4 stimulation in macrophages lacking p47^{phox} shows an increased tendency towards anti-inflammatory milieu along with an increased expression of pro-fibrotic genes.

3.5. Macrophage p47^{phox} plays a critical role in regulating angiotensin II-induced cardiac hypertrophy and fibrosis in mice

Animals were subjected to various experimental procedures as indicated in the timeline (Figure S10A). To demonstrate the importance of macrophage p47^{phox} in myocardial remodeling, WT macrophages were adoptively transferred into p47^{phox} KO mice (WT donor to KO recipient) and vice-versa (KO donor to WT recipient), followed by AngII infusion for 2 weeks. WT to WT and KO to KO mice served as controls. KO macrophages could induce cardiac hypertrophy in both WT and p47^{phox} KO recipients, as shown by altered cardiac biometrics, gross morphology and cardiomyocytes CSA in KO to WT AngII hearts (Figure S10B, Table 1 and 4A-4B). In contrast, both WT and p47^{phox} KO recipients of WT macrophages showed reduced LV hypertrophic response (Figure S10B, Table 1 and 4A-4B). Moreover, the presence of KO donor macrophages in either WT or KO recipients was enough to cause LV interstitial fibrotic deposition and elevated cardiac infiltration and increased CD206^{+} macrophages numbers by AngII (Figs. 4A, 4C and 5A-5B). However, presence of WT macrophages and collateral decrease in cardiac fibrosis and infiltration and CD206^{+} macrophage numbers protected against cardiac fibrosis and dysfunction (Figs. 4A, 4C and 5A-5B). Likewise, CD86^{+} macrophages were also observed in the adoptively transferred mice hearts to prove specifically polarization of macrophages and we found that KO donor macrophages decreased the CD86^{+}

Table 1
Cardiac geometric and functional parameters of echocardiography in Adoptive Transfer studies.

Parameter	WT to WT Saline	WT to WT AngII	WT to KO Saline	WT to KO AngII	KO to WT Saline	KO to WT AngII	KO to KO Saline	KO to KO AngII
N	6	9	5	8	7	8	6	7
HR (bpm)	507.7 ± 4.1	523.3 ± 14.8	523.7 ± 24	524 ± 9.29	518.7 ± 6.9	512 ± 7	510.3 ± 12.4	501.7 ± 3.5
SBP (mm Hg)	99 ± 2.646	128 ± 4.783**	101.7 ± 3.18	140 ± 1.786**	111.7 ± 3.283	139 ± 2.646***	117 ± 2.314	154.3 ± 2.033**@@ $
LVPW d, mm	0.82 ± 0.01	1.48 ± 0.01764**	0.84 ± 0.00	1.51 ± 0.0145**	0.89 ± 0.01	1.75 ± 0.01155**##	0.927 ± 0.01	1.83 ± 0.0260**@@ $$
LVAW d, mm	0.83 ± 0.01	1.153 ± 0.0348**	0.83 ± 0.01	1.26 ± 0.03215**	0.92 ± 0.02	1.34 ± 0.02646**##	0.963 ± 0.02	1.49 ± 0.0203**@@ $$
LVID d, mm	3.3 ± 0.038	2.933 ± 0.08479**	3.13 ± 0.04	2.863 ± 0.1322	3.14 ± 0.1	2.647 ± 0.0296**##	2.96 ± 0.053	2.65 ± 0.05
LVPW s, mm	1.19 ± 0.04	1.853 ± 0.0328**	1.28 ± 0.04	1.967 ± 0.0233**	1.32 ± 0.02	2.233 ± 0.0260**##	1.19 ± 0.046	2.373 ± 0.02**@@$$
LVAW s, mm	1.3 ± 0.023	1.61 ± 0.04041**	1.3 ± 0.049	1.677 ± 0.0203**	1.45 ± 0.03	1.937 ± 0.0291**##	1.563 ± 0.03	2.053 ± 0.04**@@$$
LVID s, mm	2.26 ± 0.03	1.823 ± 0.06888**	2.21 ± 0.02	1.74 ± 0.07937**	2.23 ± 0.04	1.537 ± 0.0546**#	2.187 ± 0.04	1.327 ± 0.05**@@$$
EF, %	63 ± 1.155	59.67 ± 1.202	61.33 ± 0.9	59.33 ± 1.453	61.3 ± 1.76	60.33 ± 1.76	65.33 ± 0.88	59 ± 2.517
LV Mass, mg	78.33 ± 2.3	114.7 ± 4.256**	81.3 ± 2.03	120.3 ± 3.48**	80.46 ± 2.887	124.67 ± 2.404**##	84 ± 2.887	134.3 ± 1.76**@@

AngII indicates Angiotensin II for 14 days. Data are expressed as the mean ± SEM; *p < 0.05, **p < 0.01 vs. respective Sham; #p < 0.05, ##p < 0.01, ###p < 0.001 WT to WT AngII vs. KO to WT AngII; @p < 0.05, @@p < 0.01, @@@p < 0.001 WT to WT AngII vs. KO to KO AngII; $p < 0.05, $$p < 0.01, $$$p < 0.001 WT to KO AngII vs. KO to KO AngII.

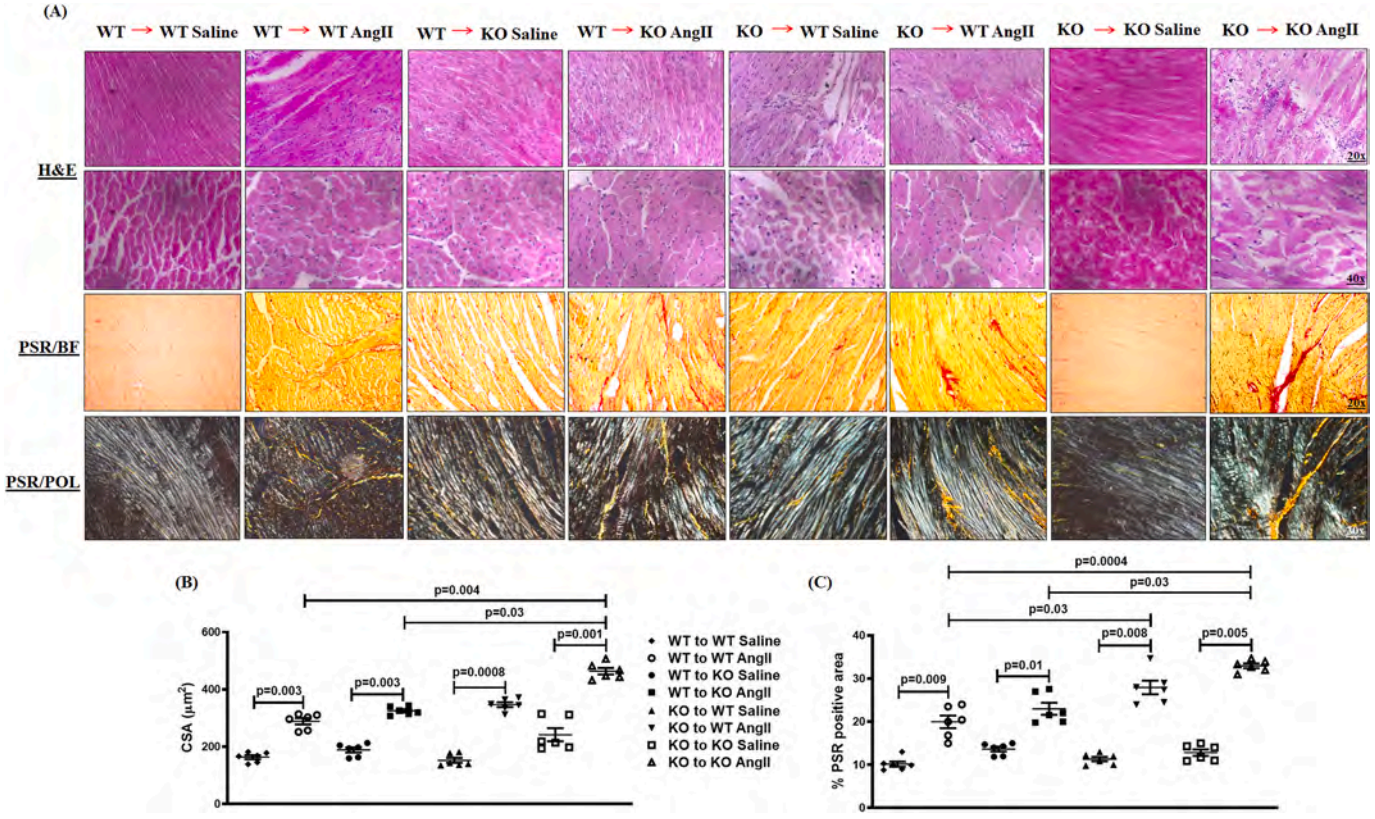

Fig. 4. Adoptive transfer of CFDA-SE labelled p47^{phox} KO BMDMs is associated with increased cardiac remodeling in mice. (A) Top to Bottom: Representative pictures of H&E stained cross sections, Picrosirius red (PSR) stained sections under both bright field and polarized light. (B) Quantification of H&E images as shown in panel (A, 2nd row). (C) Quantification of PSR images as shown in panel (A, 3rd row). Data were expressed as mean ± SEM, n = 6 per group. Total magnification, A: ×200 (except 2nd row: X400). Scale bar, A: 50 μm (except 2nd row: 25 μm). (For interpretation of the references to colour in this figure legend, the reader is referred to the Web version of this article.)

cells in the WT AngII recipient and WT donor macrophages increased the CD86^{+} cells in the KO AngII recipient (Figure S11). To further confirm, gene transcripts related to M2 macrophage was checked and it was found that KO donor macrophages in both WT and p47^{phox} KO recipient's upregulated the LV mRNA expression related to M2 macrophage signaling (IL-4, STAT6 and PPARγ) by AngII (Figure S12A-S12C). In contrast, both WT and p47^{phox} KO recipients of WT macrophages showed downregulated M2 macrophage signaling-related mRNA expression compared to WT and p47^{phox} KO recipients of KO macrophages (Figure S12A-S12C). Interestingly, KO macrophages in KO

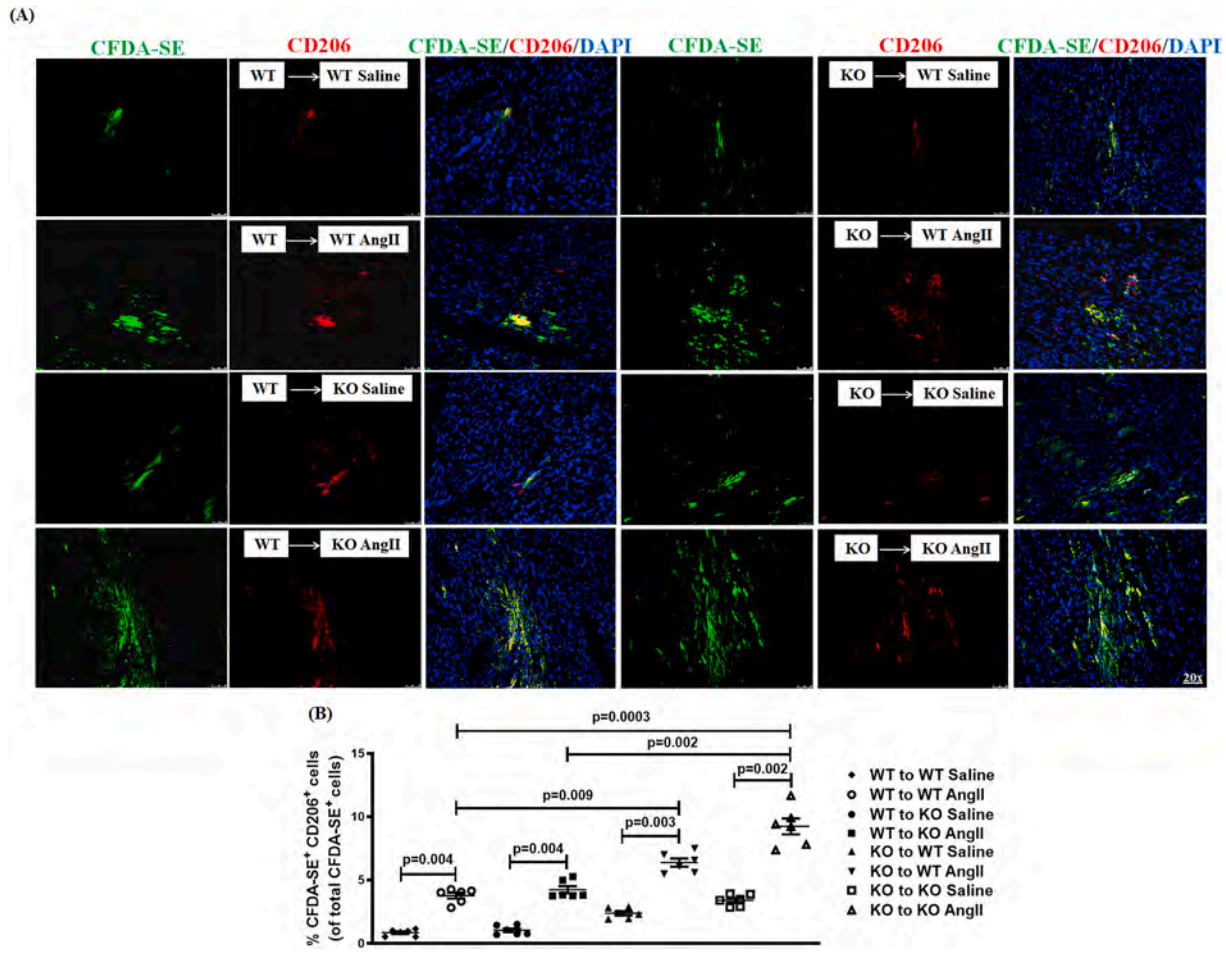

Fig. 5. Adoptive transfer of CFDA-SE-labelled WT and p47^{phox} KO BMDMs in mice. (A) Representative immunofluorescence images of CFDA-SE^{+}-CD206^{+} cells in the LV. (B) Quantification of CFDA-SE^{+}-CD206^{+} cells. DAPI was used for nuclear staining. Data were expressed as mean ± SEM, n = 6 per group. Total magnification: ×200. Scale bar: 50 μm.

recipients also showed increased LV STAT3 gene expression by AngII compared to WT macrophages in WT AngII (Figure S12D). Likewise, KO macrophages could induce cardiac fibrotic genes in both WT and p47^{phox} KO recipients, as shown by upregulated gene expression of TGF-β1, α-SMA and Collagen1 by AngII (Figure S13A-S13C). However, both WT and p47^{phox} KO recipients of WT macrophages showed reduced cardiac fibrotic gene expression in the LV compared to WT and p47^{phox} KO recipients of KO macrophages (Figure S13A-S13C). Therefore, the macrophage-specific deficiency of p47^{phox} was enough to aggregate AngII-induced cardiac hypertrophy and fibrosis in mice.

3.6. *Loss of p47^{phox} is associated with altered IL-4/STAT6/PPARγ signaling and SOCS3 expression in angiotensin II-infused mice*

It is well recognized that IL-4 stimulated M2 macrophage polarization is regulated by several transcription factors, such as PPARs and STATs [26]. Therefore, the alterations in IL4/STAT6/PPARγ pathway and SOCS3, a negative modulator of JAK/STAT axis [6,27] was studied in the LV. We found that both AngII- infused WT and KO mice showed altered mRNA expression of IL-4, PPARγ, SOCS3 and KLF4 compared to respective controls that were further enhanced in KO mice (Figure S14A and 6A-6C). In line with the IL-4 mRNA data, both AngII-infused WT and KO mice also showed elevated circulating levels of IL-4 compared to respective controls, which was significantly greater in KO mice (Figure S14B). To further confirm the data, protein expression of various STAT's phosphorylation (1, 3 and 6) was studied. We found that AngII-infused WT mice showed significant changes in protein expression of p-STAT1, p-STAT6 and SOCS3 in the LV lysates in comparison with saline-infused WT mice (Fig. 6A and 6G-6I). Likewise, AngII-infused KO mice also showed significant changes in the protein expression of p-STAT3, p-STAT6, PPARγ and SOCS3 in the LV lysates compared to saline-infused KO mice (Fig. 6A and 6H–6K). Notably, AngII-infused KO mice showed more robust changes in the p-STAT3, p-STAT6, PPARγ and SOCS3 protein expression compared to AngII-infused WT mice (Fig. 6A and 6H–6K). This is in line with the *in vitro* BMDM data, where both AngII and IL-4 treatment in WT macrophages showed increased p-STAT1 expression and KO macrophages showed increased p-STAT3 expression compared to respective controls (Figure S9). Moreover, both AngII-infused WT and KO mice also showed significant upregulation of IL-6 mRNA expression compared to respective controls that was further amplified in KO mice (Figure S14C). To further corroborate the data associated with anti-inflammatory signaling, we also observed for the changes in IRF4, OPN1 and KLF4 protein expression. Interestingly, we found that AngII-infused WT mice showed a significant increase in protein expression of KLF4 in the LV lysates compared to saline-infused WT mice (Fig. 6E and 6N). Likewise, AngII-infused KO mice also showed significant changes in the protein expression of IRF4, OPN1 and KLF4 in the LV lysates in comparison with saline-infused KO mice (Fig. 6A and 6L-6N). Although, AngII-infused KO mice showed more prominent changes in protein expression of IRF4, OPN1 and KLF4 compared to AngII-infused WT mice (Fig. 6A and 6L-6N). In agreement with the AngII data, we found that both TAC-induced WT and KO mice showed a significant increase in mRNA expression of IL-4 and IL-6 in the LV lysates compared to respective controls (Fig. 6D and S7G). However, no

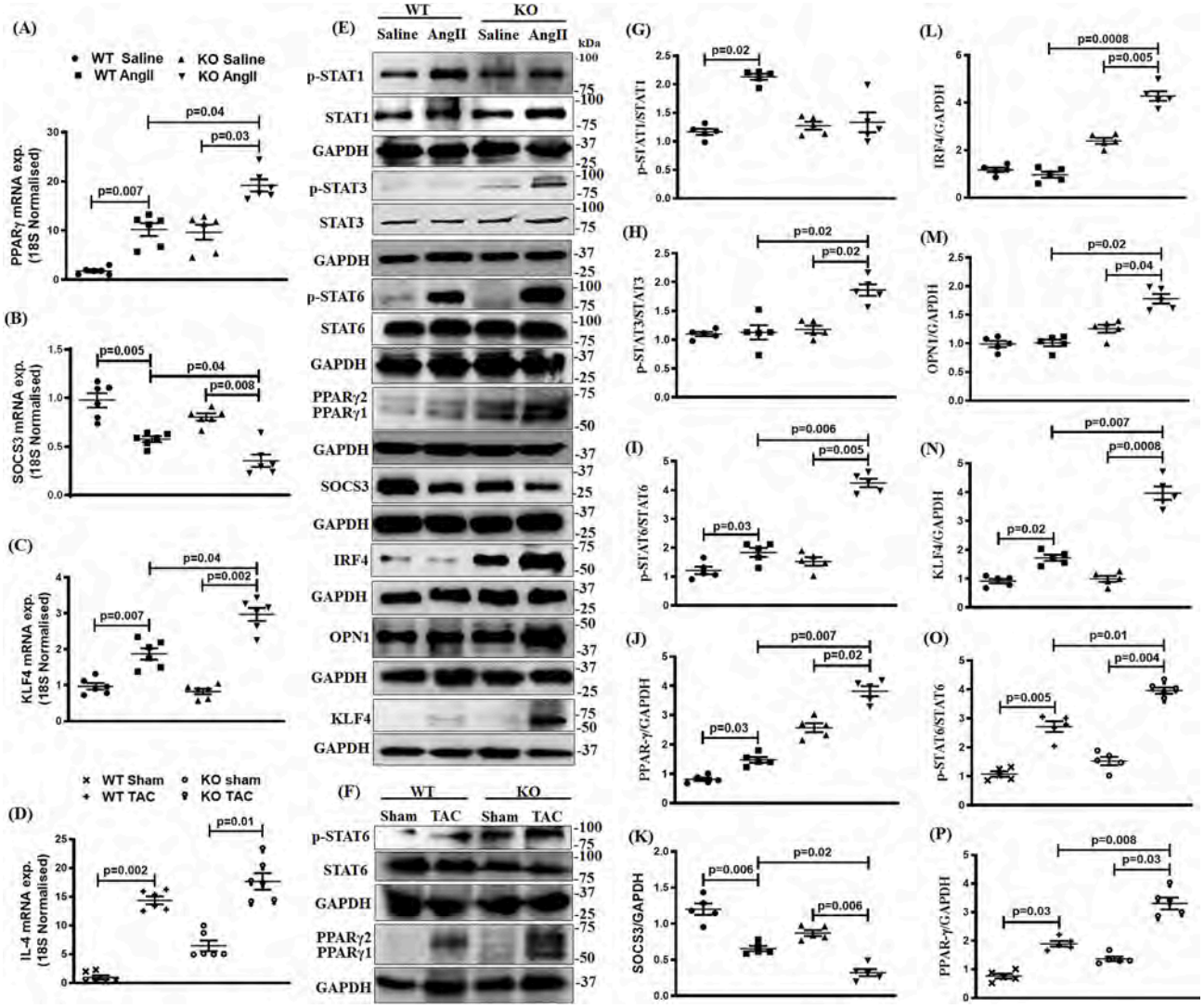

Fig. 6. Pressure-overload in p47^{phox} KO mice leads to increased IL-4/STAT6/PPARγ signaling. (A–D) Relative mRNA expression of PPARγ (A), SOCS3 (B), KLF4 (C) in the LV tissue lysates of saline- or AngII-infused mice and IL-4 (D) in LV tissue lysates of sham or TAC-induced mice by Real-time PCR. 18S was used as a loading control. (E) Representative Western blots images of various proteins (STAT1, STAT3, STAT6, PPARγ, SOCS3, IRF4, OPN1 and KLF4) in the LV tissue lysates of saline- or AngII-infused mice. (F) Representative Western blots images of various proteins (STAT6 and PPARγ) in the LV tissue lysates of sham or TAC-induced mice. (G–P) Quantification of Western blot images as shown in panel (E–F) using Image J software. The densitometry values were normalized to that of total protein or GAPDH and the value is presented as a fold change. GAPDH was used as loading control. Data were expressed as mean ± SEM, n = 6 per group. The blots are representatives of five similar experiments.

significant change in mRNA expression of IL-4 and IL-6 was observed between TAC-induced WT and KO mice (Fig. 6D and S7G). Further, we also found that both TAC-induced WT and KO mice showed significant upregulation of STAT6 phosphorylation compared to respective controls (Fig. 6F and 6O). Besides, TAC-induced KO mice also showed significant upregulation of PPARγ protein expression compared to sham KO mice (Fig. 6F and P). However, TAC-induced WT mice did not show upregulation of PPARγ protein expression compared to WT Sham mice (Fig. 6F and 6P). Notably, TAC in KO mice showed more prominent changes in STAT6 phosphorylation and PPARγ protein expression compared to WT TAC mice (Fig. 6F and 6O–6P). These findings indicate that p47^{phox} limits cardiac hypertrophy and fibrosis by modulating the IL-4/STAT6/PPARγ pathway and SOCS3 expression.

4. Discussion

Several immune cells such as monocytes and macrophages play a critical role in initiating and propagating pathological cardiac remodeling by regulating cardiomyocyte and non-cardiomyocyte responses [7]. The contribution of macrophage p47^{phox} in this process remains debatable. In this study, we address the cardiac hypertrophic and fibrotic response during cardiac pressure-overload and identify macrophage p47^{phox} as a potent contributor to cardiac hypertrophy and interstitial fibrosis by regulating IL-4/STAT6/PPARγ signaling axis and SOCS3 expression.

The absence of p47^{phox} is associated with RAS activation, contributing to blood pressure elevation in a ROS-independent manner [13]. Accordingly, we also found elevated SBP in KO mice. However, it contrasts with other studies [28,29], where the loss of p47^{phox} leads to decreased SBP, and this could be possible because of the difference in KO mice age and dose and duration of AngII-infused. Subsequently, persistent high blood pressure load usually leads to interstitial or non-adaptive cardiac fibrosis, which can cause LVH and diastolic/systolic dysfunction [30]. Here, we observed that AngII-infused p47^{phox} KO mice showed increased LV interstitial collagen deposition and further substantiated by altered pro-fibrotic genes. Most etiologies

of heart disease involve pathological myocardial remodeling characterized by cardiac fibroblasts-derived excessive accumulation of ECM proteins, thereby reducing tissue compliance and accelerates the progression to cardiac failure [31]. Accordingly, AngII infusion in p47^{phox} KO mice is associated with upregulated α-SMA in the LV, indicating myofibroblasts activation and worsening cardiac fibrosis. This is in line with the previous reports [12], where the lack of p47^{phox} has been shown to promote myocardial fibrosis subjected to biomechanical stress. However, our finding contrasts with the previous studies [32–34], where the loss of Nox2 is associated with reduced interstitial fibrosis, and this difference could be due to cell-specific effects of Nox, acute and chronic response of the pressure-overload.

Moreover, AngII-infused p47^{phox} KO mice also showed increased circulating IL-4 levels in line with the reported literature suggesting chronically elevated IL-4 induces cardiac fibrosis [24]. In fact, IL-4 has been shown to play a crucial role in the prognosis of dilated cardiomyopathy [24]. Taken together, p47^{phox} plays a significant role in regulating the various aspects of AngII-mediated cardiac hypertrophy.

Further, we also employed another model for pressure-overload (TAC) to exclude the observed phenotype's model specificity. Indeed, TAC-induced p47^{phox} KO mice showed increased cardiac remodeling and dysfunction. Thus, a similar phenotype in both the pressure-overload models marks the importance of p47^{phox} in directing myocardial remodeling irrespective of the hypertrophic stimuli. Cardiac remodeling responses of the two models were assessed only after 14 days since we focused on the difference of cardiac remodeling responses of the two types of models. Also, the time points are very appropriate to investigate the cellular response such as hypertrophy, ECM deposition, and secretion of anti-inflammatory mediators in both models [3,35–37]. One of the limitation of the present study is its short duration and therefore the interpretations may be more applicable to the developmental phase of hypertrophy when compared to chronic heart failure setting. However, it will be very interesting to see how macrophage p47^{phox} might orchestrate cardiac remodeling during heart failure.

AngII is a critical player in mediating hypertension-induced target organ damage and hypertrophy besides a potent inducer of inflammatory state [6]. Moreover, phosphorylation will be an crucial aspect, since it is an important mechanism of activity regulation as also seen previously [38] in the case of p47^{phox}, where Angiotensin II mediated p47^{phox} phosphorylation by PKC and other kinases and its translocation to the plasma membrane along with other subunits and regulates different signaling involving apoptosis, fibrosis, and inflammation etc. thereby, effecting cardiovascular remodeling. However, since in the present study p47^{phox} was deleted with no significant protein expression, analysis of phosphorylation would have not yielded any significant outcome. The present study analysed the effect of the protein itself. However, it will be very interesting to monitor the disease progression in functionally phosphorylation inactive mutants. Also, many sites are known to be phosphorylated in p47^{phox} that may regulate its activity [39,40]. Therefore it will be important to first prioritize the phosphorylation sites to be monitored. Here, we observed that AngII-infused p47^{phox} KO mice showed increased LV infiltration and proliferation (high Ki-67^{+} cells) of leukocytes and were found to be particularly enriched in Mac3^{+} cells, indicating robust macrophage infiltration in LV compared to AngII-infused p47^{phox} expressed mice. Likewise, macrophages play a critical role in innate immune system activation and their function, thus mediating tissue homeostasis, immunomodulation, and disease pathogenesis [41]. Macrophage rewiring (towards M1, pro-inflammatory or M2, anti-inflammatory/pro-fibrotic type) results in macrophages' dual role in tissue inflammation and healing [42]. Importantly, it has been shown that M2 macrophages contribute to cardiac fibrosis in hypertension [43] and post-MI [44] while blocking the activation of M2 macrophages is linked with reduced fibrosis and heart failure [1,43]. Therefore, we noted the pro-and anti-inflammatory balance under the setting of hypertension in both WT and p47^{phox} KO mice.

Interestingly, LV of AngII-infused p47^{phox} KO mice showed an increased tendency towards anti-inflammatory milieu. Indeed, our finding that macrophages contribute to hypertensive myocardial remodeling is in line with previous studies [45], where the role of activated macrophages in failure-prone hypertrophied hearts is demonstrated. Additionally, a multi-cytokine array was performed to explore the circulating levels of various immunokines indicative of macrophage activation or vital for tissue invasion were also significantly elevated in AngII-infused p47^{phox} KO mice, indicating its essential role in immunomodulation. Overall, these data suggest that p47^{phox} limits macrophage infiltration in the pressure-overloaded heart.

Consistent with our data showing elevated plasma IL-4 levels in hypertensive mice and previous reports related to the pivotal role for IL-4 in AngII–induced cardiac damage [24]and p47^{phox} KO macrophages being hyperresponsive to IL-4[46]. We performed *in vitro* study of BMDMs and found that p47^{phox} KO macrophages (M0) stimulated with both AngII and IL-4 showed highly upregulated anti-inflammatory/M2 macrophage markers and slightly downregulated pro-inflammatory/M1 macrophage markers compared to both AngII and IL-4 treated WT macrophages (M0). These results indicate that p47^{phox} possibly restrains AngII mediated anti-inflammatory/M2 macrophage activation, thereby maintaining pro-and anti-inflammatory homeostasis and; AngII and IL-4 mediated synergistic effect on cardiac remodeling.

Since, the p47^{phox} KO mice used in the study is a global KO mouse and importantly, the expression of p47^{phox} predominates in various myeloid cells [47]. Therefore, to corroborate the regulatory role of p47^{phox} specific to macrophages, adoptive transfer studies were performed. Intriguingly, CFDA-SE labelled BMDMs transplantation from p47^{phox} KO mice to WT mice showed increased levels of M2 type macrophages in the LV and augmented cardiac remodeling after AngII infusion. These data further support the notion that macrophage p47^{phox} has a dynamic role in mediating hypertensive cardiac remodeling.

Furthermore, the cytokines that regulate macrophage phenotype signal primarily through the JAK-STAT pathway are associated with the activation of various transcription factors, which dictate pro- and anti-inflammatory macrophage balance [48]. STAT6 is the crucial transcription factor in IL-4 and IL-13–mediated macrophage rewiring towards anti-inflammatory macrophage phenotype [49]. In fact, AngII-infused p47^{phox} KO mice which demonstrated increased LV anti-inflammatory macrophage levels were associated with upregulated STAT6 phosphorylation (Y641) and subsequent induction of the genes related with alternate activation of macrophages such as Arg-1, Mrc-1 and Ym-1 compared to AngII-infused WT mice. Similarly, crosstalk between the IL-4–STAT6 and PPAR-γ axis modulates the anti-inflammatory macrophage phenotype [49]. Hence, we observed the changes in PPAR-γ and were found to be upregulated in the LV of AngII-infused p47^{phox} KO mice. These changes were also corroborated in TAC-treated p47^{phox} KO mice. IL-6 induced STAT3 binds to IL-4Rα promoter, thus, promoting IL-4-dependent STAT6 activation [50]. In line with this study, AngII-infused p47^{phox} KO mice also showed increased IL-6 levels and STAT3 phosphorylation (Y705), thereby further strengthening IL-4/STAT6/PPARγ mediated anti-inflammatory milieu. These findings are in contrast with one of the general notions that IL-6 acts as a pro-inflammatory cytokine [51]. However, in line with our results, it was recently reported that IL-6 signaling is associated with macrophage rewiring toward alternative activation [51]. Since, STAT3 activation is a prerequisite for skewing macrophages toward the galectin-3^{hi} reparative M2 phenotype and transcriptional activation of the Spp1 gene, encoding OPN1 [52]. Here, we observed the changes in OPN1 protein expression and found it highly upregulated in LV of AngII-infused p47^{phox} KO mice. It was interesting to see that Ang-II activates STAT-1 only in WT mice and not in p47^{phox} deficient animals. Since STAT-1 primarily activates the M1 phenotype [53], this also explains how non-activation of STAT-1 in p47^{phox} deficient mice can promote M2 phenotype, as reported earlier also [54]. P47^{phox} promotes STAT-1 activation [55], however, the role of other p47^{phox} dependent mediators in STAT-1 regulation cannot be ruled out. Moreover, it has

been shown that IL-4 stimulation in p47^{phox} deficient macrophages is associated with hyper STAT6 phosphorylation [46]. Thus, in line with the *in vivo* data, we also found that both AngII and IL-4 treated p47^{phox} KO BMDMs showed higher STAT6 phosphorylation (Y641) levels, further emphasizing the concept of hyperactive IL-4 signaling in p47^{phox} background.

Interestingly, AngII-infused p47^{phox} KO mice also showed increased expression of transcriptional regulators such as IRF4 and KLF4, indicating increased M2 subtype polarization, which agrees with the previous study [49]. Moreover, it was demonstrated that myeloid cell-specific disruption of SOCS3, the negative regulator of the IL-6/STAT3 and IL-4/STAT6 axis, skews macrophages towards an M2 phenotype [27,56]. Accordingly, we also found reduced expression of SOCS3 mRNA and protein in AngII-infused p47^{phox} KO mice compared to AngII-infused WT mice. Thus, indicating that such robust cardiac remodeling in response to pressure-overload in p47^{phox} KO mice is at least in part is mediated by macrophage SOCS3 downregulation. Although, the absolute downregulation of SOCS3 by AngII in p47^{phox} KO mice is not that great when compared to AngII-infused WT mice and the statistical significance is only single star ($p = 0.02$). However, to ascertain whether such subtle changes are transmitted downstream and affect disease progression, additional experiments need to be performed.

5. Conclusions

Overall, the present study provide conclusive evidence that profibrotic signaling through macrophage p47^{phox} modulates cardiac hypertrophy, ECM remodeling and inflammation in the mouse heart during pressure-overload. Mechanistically, lack of p47^{phox} in macrophages results in increased tendency towards anti-inflammatory/M2 macrophage phenotype by hyperactivating the STAT3 and STAT6 pathway and downregulating SOCS3 expression, which could be an attractive therapeutic strategy for treating HHD.

Acknowledgements

Grant support to MKB from Council of Scientific & Industrial Research-Central Drug Research Institute, India (CSIR-CDRI); Department of Science & Technology (DST) and Department of Biotechnology (DBT), India is acknowledged. Award of Senior Research fellowships to SSR and HA from ICMR is gratefully acknowledged. Authors also acknowledge the excellent technical help of Mr. C.P Pandey for microscopy and Mr. Pankaj Shukla for echocardiography experiments. CDRI manuscript communication number is 10204.

Appendix A. Supplementary data

Supplementary data to this article can be found online at https://doi.org/10.1016/j.freeradbiomed.2021.03.007.

Author contributions

S.S.R. did majority of experiments and data compilation and prepared draft manuscript, H.A. carried out *in vitro* BMDM and some animal experiments, A.J. did some BMDM experiments, K.J. helped in the p47^{phox} animal studies, M.D. provide critical inputs for the study, M.K.B. is responsible for the overall concept, project generation and conduct and finalization of the manuscript.

Disclosures

None.

References

[1] M. Yang, J. Zheng, Y. Miao, Y. Wang, W. Cui, J. Guo, S. Qiu, Y. Han, L. Jia, H. Li, J. Cheng, J. Du, Serum-glucocorticoid regulated kinase 1 regulates alternatively activated macrophage polarization contributing to angiotensin II-induced inflammation and cardiac fibrosis, Arterioscler. Thromb. Vasc. Biol. 32 (2012) 1675–1686.

[2] X. Xie, H.L. Bi, S. Lai, Y.L. Zhang, N. Li, H.J. Cao, L. Han, H.X. Wang, H.H. Li, The immunoproteasome catalytic beta5i subunit regulates cardiac hypertrophy by targeting the autophagy protein ATG5 for degradation, Sci Adv 5 (2019) eaau0495.

[3] E. Matsumoto, S. Sasaki, H. Kinoshita, T. Kito, H. Ohta, M. Konishi, K. Kuwahara, K. Nakao, N. Itoh, Angiotensin II-induced cardiac hypertrophy and fibrosis are promoted in mice lacking Fgf 16, Gene Cell. 18 (2013) 544–553.

[4] J. Han, S. Ye, C. Zou, T. Chen, J. Wang, J. Li, L. Jiang, J. Xu, W. Huang, Y. Wang, G. Liang, Angiotensin II causes biphasic STAT3 activation through TLR4 to initiate cardiac remodeling, Hypertension 72 (2018) 1301–1311.

[5] Y. Matsui, N. Jia, H. Okamoto, S. Kon, H. Onozuka, M. Akino, L. Liu, J. Morimoto, S.R. Rittling, D. Denhardt, A. Kitabatake, T. Uede, Role of osteopontin in cardiac fibrosis and remodeling in angiotensin II-induced cardiac hypertrophy, Hypertension 43 (2004) 1195–1201.

[6] S. Heymans, M.F. Corsten, W. Verhesen, P. Carai, R.E. van Leeuwen, K. Custers, T. Peters, M. Hazebroek, L. Stoger, E. Wijnands, B.J. Janssen, E.E. Creemers, Y. M. Pinto, D. Grimm, N. Schurmann, E. Vigorito, T. Thum, F. Stassen, X. Yin, M. Mayr, L.J. de Windt, E. Lutgens, K. Wouters, M.P. de Winther, S. Zacchigna, M. Giacca, M. van Bilsen, A.P. Papageorgiou, B. Schroen, Macrophage microRNA-155 promotes cardiac hypertrophy and failure, Circulation 128 (2013) 1420–1432.

[7] M. Hulsmans, F. Sam, M. Nahrendorf, Monocyte and macrophage contributions to cardiac remodeling, J. Mol. Cell. Cardiol. 93 (2016) 149–155.

[8] Y. Li, C. Zhang, Y. Wu, Y. Han, W. Cui, L. Jia, L. Cai, J. Cheng, H. Li, J. Du, Interleukin-12p35 deletion promotes CD4 T-cell-dependent macrophage differentiation and enhances angiotensin II-Induced cardiac fibrosis, Arterioscler. Thromb. Vasc. Biol. 32 (2012) 1662–1674.

[9] V. Byles, A.J. Covarrubias, I. Ben-Sahra, D.W. Lamming, D.M. Sabatini, B. D. Manning, T. Horng, The TSC-mTOR pathway regulates macrophage polarization, Nat. Commun. 4 (2013) 2834.

[10] N. Kapoor, J. Niu, Y. Saad, S. Kumar, T. Sirakova, E. Becerra, X. Li, P. E. Kolattukudy, Transcription factors STAT6 and KLF4 implement macrophage polarization via the dual catalytic powers of MCPIP, J. Immunol. 194 (2015) 6011–6023.

[11] H. Qin, A.T. Holdbrooks, Y. Liu, S.L. Reynolds, L.L. Yanagisawa, E.N. Benveniste, SOCS3 deficiency promotes M1 macrophage polarization and inflammation, J. Immunol. 189 (2012) 3439–3448.

[12] V.B. Patel, Z. Wang, D. Fan, P. Zhabyeyev, R. Basu, S.K. Das, W. Wang, J. Desaulniers, S.M. Holland, Z. Kassiri, G.Y. Oudit, Loss of p47phox subunit enhances susceptibility to biomechanical stress and heart failure because of dysregulation of cortactin and actin filaments, Circ. Res. 112 (2013) 1542–1556.

[13] K. Grote, M. Ortmann, G. Salguero, C. Doerries, U. Landmesser, M. Luchtefeld, R. P. Brandes, W. Gwinner, T. Tschernig, E.G. Brabant, A. Klos, A. Schaefer, H. Drexler, B. Schieffer, Critical role for p47phox in renin-angiotensin system activation and blood pressure regulation, Cardiovasc. Res. 71 (2006) 596–605.

[14] A. Jaiswal, S.S. Reddy, M. Maurya, P. Maurya, M.K. Barthwal, MicroRNA-99a mimics inhibit M1 macrophage phenotype and adipose tissue inflammation by targeting TNFalpha, Cell. Mol. Immunol. 16 (2019) 495–507.

[15] C.K. Huang, L. Zhan, M.O. Hannigan, Y. Ai, T.L. Leto, P47(phox)-deficient NADPH oxidase defect in neutrophils of diabetic mouse strains, C57BL/6J-m db/db and db/+, J. Leukoc. Biol. 67 (2000) 210–215.

[16] M. Dhiman, N.J. Garg, P47phox-/- mice are compromised in expansion and activation of CD8+ T cells and susceptible to Trypanosoma cruzi infection, PLoS Pathog. 10 (2014), e1004516.

[17] M. Zi, N. Stafford, S. Prehar, F. Baudoin, D. Oceandy, X. Wang, T. Bui, M. Shaheen, L. Neyses, E.J. Cartwright, Cardiac hypertrophy or failure? - a systematic evaluation of the transverse aortic constriction model in C57BL/6NTac and C57BL/6J substrains, Curr Res Physiol 1 (2019) 1–10.

[18] L.H. Wei, X.R. Huang, Y. Zhang, Y.Q. Li, H.Y. Chen, B.P. Yan, C.M. Yu, H.Y. Lan, Smad 7 inhibits angiotensin II-induced hypertensive cardiac remodelling, Cardiovasc. Res. 99 (2013) 665–673.

[19] S.S. Reddy, H. Agarwal, M.K. Barthwal, Cilostazol ameliorates heart failure with preserved ejection fraction and diastolic dysfunction in obese and non-obese hypertensive mice, J. Mol. Cell. Cardiol. 123 (2018) 46–57.

[20] R. Tavakoli, S. Nemska, P. Jamshidi, M. Gassmann, N. Frossard, Technique of minimally invasive transverse aortic constriction in mice for induction of left ventricular hypertrophy, JoVE (2017).

[21] S.S. Reddy, P. Chauhan, P. Maurya, D. Saini, P.P. Yadav, M.K. Barthwal, Coagulin-L ameliorates TLR4 induced oxidative damage and immune response by regulating mitochondria and NOX-derived ROS, Toxicol. Appl. Pharmacol. 309 (2016) 87–100.

[22] L. Miao, X. Shen, M. Whiteman, H. Xin, Y. Shen, X. Xin, P.K. Moore, Y.Z. Zhu, Hydrogen sulfide mitigates myocardial infarction via promotion of mitochondrial biogenesis-dependent M2 polarization of macrophages, Antioxidants Redox Signal. 25 (2016) 268–281.

[23] L. Zhao, G. Cheng, R. Jin, M.R. Afzal, A. Samanta, Y.T. Xuan, M. Girgis, H.K. Elias, Y. Zhu, A. Davani, Y. Yang, X. Chen, S. Ye, O.L. Wang, L. Chen, J. Hauptman, R. J. Vincent, B. Dawn, Deletion of interleukin-6 attenuates pressure overload-induced left ventricular hypertrophy and dysfunction, Circ. Res. 118 (2016) 1918–1929.

[24] H. Peng, Z. Sarwar, X.P. Yang, E.L. Peterson, J. Xu, B. Janic, N. Rhaleb, O. A. Carretero, N.E. Rhaleb, Profibrotic role for interleukin-4 in cardiac remodeling and dysfunction, Hypertension 66 (2015) 582–589.
[25] A.L. Wurster, T. Tanaka, M.J. Grusby, The biology of Stat 4 and Stat6, Oncogene 19 (2000) 2577–2584.
[26] H. Li, T. Jiang, M.Q. Li, X.L. Zheng, G.J. Zhao, Transcriptional regulation of macrophages polarization by MicroRNAs, Front. Immunol. 9 (2018) 1175.
[27] D. Pastuszak-Lewandoska, D. Domanska-Senderowska, A. Antczak, J. Kordiak, P. Gorski, K.H. Czarnecka, M. Migdalska-Sek, E. Nawrot, J.M. Kiszalkiewicz, E. Brzezianska-Lasota, The expression levels of IL-4/IL-13/STAT6 signaling pathway genes and SOCS3 could help to differentiate the histopathological subtypes of non-small cell lung carcinoma, Mol. Diagn. Ther. 22 (2018) 621–629.
[28] U. Landmesser, H. Cai, S. Dikalov, L. McCann, J. Hwang, H. Jo, S.M. Holland, D. G. Harrison, Role of p47(phox) in vascular oxidative stress and hypertension caused by angiotensin II, Hypertension 40 (2002) 511–515.
[29] J.D. Fangfei Liu, Jian-Mei Li, KNOCKOUT P47PHOX REDUCES ANGIOTENSIN IIINDUCED CARDIAC OXIDATIVE STRESS AND HYPERTROPHY, 2017.
[30] F. Ma, J. Feng, C. Zhang, Y. Li, G. Qi, H. Li, Y. Wu, Y. Fu, Y. Zhao, H. Chen, J. Du, H. Tang, The requirement of CD8+ T cells to initiate and augment acute cardiac inflammatory response to high blood pressure, J. Immunol. 192 (2014) 3365–3373.
[31] J.G. Travers, F.A. Kamal, J. Robbins, K.E. Yutzey, B.C. Blaxall, Cardiac fibrosis: the fibroblast awakens, Circ. Res. 118 (2016) 1021–1040.
[32] A. Sirker, M. Zhang, C. Murdoch, A.M. Shah, Involvement of NADPH oxidases in cardiac remodelling and heart failure, Am. J. Nephrol. 27 (2007) 649–660.
[33] A. Sirker, C.E. Murdoch, A. Protti, G.J. Sawyer, C.X. Santos, D. Martin, X. Zhang, A. C. Brewer, M. Zhang, A.M. Shah, Cell-specific effects of Nox2 on the acute and chronic response to myocardial infarction, J. Mol. Cell. Cardiol. 98 (2016) 11–17.
[34] Y.H. Looi, D.J. Grieve, A. Siva, S.J. Walker, N. Anilkumar, A.C. Cave, M. Marber, M.J. Monaghan, A.M. Shah, Involvement of Nox2 NADPH oxidase in adverse cardiac remodeling after myocardial infarction, Hypertension 51 (2008) 319–325.
[35] S. Kudo, K. Satoh, M. Nogi, K. Suzuki, S. Sunamura, J. Omura, N. Kikuchi, R. Kurosawa, T. Satoh, T. Minami, S. Ikeda, S. Miyata, H. Shimokawa, SmgGDS as a crucial mediator of the inhibitory effects of statins on cardiac hypertrophy and fibrosis: novel mechanism of the pleiotropic effects of statins, Hypertension 67 (2016) 878–889.
[36] J. You, J. Wu, Q. Zhang, Y. Ye, S. Wang, J. Huang, H. Liu, X. Wang, W. Zhang, L. Bu, J. Li, L. Lin, J. Ge, Y. Zou, Differential cardiac hypertrophy and signaling pathways in pressure versus volume overload, Am. J. Physiol. Heart Circ. Physiol. 314 (2018) H552–H562.
[37] J. Zhong, R. Basu, D. Guo, F.L. Chow, S. Byrns, M. Schuster, H. Loibner, X.H. Wang, J.M. Penninger, Z. Kassiri, G.Y. Oudit, Angiotensin-converting enzyme 2 suppresses pathological hypertrophy, myocardial fibrosis, and cardiac dysfunction, Circulation 122 (717–28) (2010), 18 pp. following 728.
[38] T.M. Paravicini, R.M. Touyz, NADPH oxidases, reactive oxygen species, and hypertension: clinical implications and therapeutic possibilities, Diabetes Care 31 (Suppl 2) (2008) S170–S180.
[39] C.R. Hoyal, A. Gutierrez, B.M. Young, S.D. Catz, J.H. Lin, P.N. Tsichlis, B.M. Babior, Modulation of p47PHOX activity by site-specific phosphorylation: akt-dependent activation of the NADPH oxidase, Proc. Natl. Acad. Sci. U. S. A. 100 (2003) 5130–5135.
[40] D.N. Meijles, L.M. Fan, B.J. Howlin, J.M. Li, Molecular insights of p47phox phosphorylation dynamics in the regulation of NADPH oxidase activation and superoxide production, J. Biol. Chem. 289 (2014) 22759–22770.
[41] C.V. Lewis, A. Vinh, H. Diep, C.S. Samuel, G.R. Drummond, B.K. Kemp-Harper, Distinct redox signalling following macrophage activation influences profibrotic activity, J Immunol Res 2019 (2019) 1278301.
[42] D.A. White, Y. Su, P. Kanellakis, H. Kiriazis, E.F. Morand, R. Bucala, A.M. Dart, X. M. Gao, X.J. Du, Differential roles of cardiac and leukocyte derived macrophage migration inhibitory factor in inflammatory responses and cardiac remodelling post myocardial infarction, J. Mol. Cell. Cardiol. 69 (2014) 32–42.
[43] N. Glezeva, V. Voon, C. Watson, S. Horgan, K. McDonald, M. Ledwidge, J. Baugh, Exaggerated inflammation and monocytosis associate with diastolic dysfunction in heart failure with preserved ejection fraction: evidence of M2 macrophage activation in disease pathogenesis, J. Card. Fail. 21 (2015) 167–177.
[44] P. Shivshankar, G.V. Halade, C. Calhoun, G.P. Escobar, A.J. Mehr, F. Jimenez, C. Martinez, H. Bhatnagar, C.H. Mjaatvedt, M.L. Lindsey, C.J. Le Saux, Caveolin-1 deletion exacerbates cardiac interstitial fibrosis by promoting M2 macrophage activation in mice after myocardial infarction, J. Mol. Cell. Cardiol. 76 (2014) 84–93.
[45] U.C. Sharma, S. Pokharel, T.J. van Brakel, J.H. van Berlo, J.P. Cleutjens, B. Schroen, S. Andre, H.J. Crijns, H.J. Gabius, J. Maessen, Y.M. Pinto, Galectin-3 marks activated macrophages in failure-prone hypertrophied hearts and contributes to cardiac dysfunction, Circulation 110 (2004) 3121–3128.
[46] L. Yi, Q. Liu, M.S. Orandle, S. Sadiq-Ali, S.M. Koontz, U. Choi, F.J. Torres-Velez, S. H. Jackson, p47(phox) directs murine macrophage cell fate decisions, Am. J. Pathol. 180 (2012) 1049–1058.
[47] I. Al Ghouleh, D.N. Meijles, S. Mutchler, Q. Zhang, S. Sahoo, A. Gorelova, J. Henrich Amaral, A.I. Rodriguez, T. Mamonova, G.J. Song, A. Bisello, P. A. Friedman, M.E. Cifuentes-Pagano, P.J. Pagano, Binding of EBP50 to Nox organizing subunit p47phox is pivotal to cellular reactive species generation and altered vascular phenotype, Proc. Natl. Acad. Sci. U. S. A. 113 (2016) E5308–E5317.
[48] D. Carneros, E.M. Santamaria, E. Larequi, J.M. Velez-Ortiz, M. Reboredo, U. Mancheno, M.J. Perugorria, P. Navas, M. Romero-Gomez, J. Prieto, S. Hervas-Stubbs, M. Bustos, Cardiotrophin-1 is an anti-inflammatory cytokine and promotes IL-4-induced M2 macrophage polarization, Faseb. J. 33 (2019) 7578–7587.
[49] D. Tugal, X. Liao, M.K. Jain, Transcriptional control of macrophage polarization, Arterioscler. Thromb. Vasc. Biol. 33 (2013) 1135–1144.
[50] J. Mauer, B. Chaurasia, J. Goldau, M.C. Vogt, J. Ruud, K.D. Nguyen, S. Theurich, A. C. Hausen, J. Schmitz, H.S. Bronneke, E. Estevez, T.L. Allen, A. Mesaros, L. Partridge, M.A. Febbraio, A. Chawla, F.T. Wunderlich, J.C. Bruning, Signaling by IL-6 promotes alternative activation of macrophages to limit endotoxemia and obesity-associated resistance to insulin, Nat. Immunol. 15 (2014) 423–430.
[51] L.M. Sanmarco, N.E. Ponce, L.M. Visconti, N. Eberhardt, M.G. Theumer, A. R. Minguez, M.P. Aoki, IL-6 promotes M2 macrophage polarization by modulating purinergic signaling and regulates the lethal release of nitric oxide during Trypanosoma cruzi infection, Biochim. Biophys. Acta (BBA) - Mol. Basis Dis. 1863 (2017) 857–869.
[52] K. Shirakawa, J. Endo, M. Kataoka, Y. Katsumata, N. Yoshida, T. Yamamoto, S. Isobe, H. Moriyama, S. Goto, H. Kitakata, T. Hiraide, K. Fukuda, M. Sano, IL (Interleukin)-10-STAT3-Galectin-3 Axis is essential for osteopontin-producing reparative macrophage polarization after myocardial infarction, Circulation 138 (2018) 2021–2035.
[53] M. Orecchioni, Y. Ghosheh, A.B. Pramod, K. Ley, Macrophage polarization: different gene signatures in M1(LPS+) vs. Classically and M2(LPS-) vs. Alternatively activated macrophages, Front. Immunol. 10 (2019) 1084.
[54] S. Kemmner, Q. Bachmann, S. Steiger, G. Lorenz, M. Honarpisheh, O. Foresto-Neto, S. Wang, J. Carbajo-Lozoya, V. Alt, C. Schulte, S. Chmielewski, H.A.R. Bluyssen, U. Heemann, M. Baumann, M. Lech, C. Schmaderer, STAT1 regulates macrophage number and phenotype and prevents renal fibrosis after ischemia-reperfusion injury, Am. J. Physiol. Ren. Physiol. 316 (2019) F277–F291.
[55] C.S. Yang, J.J. Kim, S.J. Lee, J.H. Hwang, C.H. Lee, M.S. Lee, E.K. Jo, TLR3-triggered reactive oxygen species contribute to inflammatory responses by activating signal transducer and activator of transcription-1, J. Immunol. 190 (2013) 6368–6377.
[56] X.L. Fu, W. Duan, C.Y. Su, F.Y. Mao, Y.P. Lv, Y.S. Teng, P.W. Yu, Y. Zhuang, Y. L. Zhao, Interleukin 6 induces M2 macrophage differentiation by STAT3 activation that correlates with gastric cancer progression, Cancer Immunol. Immunother. 66 (2017) 1597–1608.